J. Fluid Mech. (2004), *vol.* 514, *pp.* 231–270.
DOI: 10.1017/S0022112004000266 Printed in the United Kingdom

Direct simulation of non-premixed flame extinction in a methane–air jet with reduced chemistry

By C. PANTANO

Graduate Aeronautical Laboratories, California Institute of Technology,
1200 E. California Blvd., 105-50, Pasadena, CA 91125, USA
cpantano@galcit.caltech.edu

(Received 10 November 2003 and in revised form 6 April 2004)

A three-dimensional direct numerical simulation (DNS) study of a spatially evolving planar turbulent reacting jet is reported. Combustion of methane with air is modelled using a four-step reduced mechanism in the non-premixed regime. A total of eight chemical species are integrated in time along with the fluid mechanical fields. The solution of the compressible Navier–Stokes equations is obtained numerically for moderately low Mach number. A large computational grid, with 100 million grid points, is required in order to resolve the flame. The cold flow Reynolds number is 3000. The focus of the study is to investigate the dynamics of extinction fronts in three-dimensional turbulent flows. A novel data reduction and identification algorithm was developed to postprocess the large DNS database and extract the shape of the evolving flame surface including its edges and their propagation velocity. The joint probability density function (p.d.f.) of edge velocity and scalar dissipation was obtained and the results indicate that the three-dimensional flame edges propagate with a velocity that is largely controlled by the local rate of scalar dissipation, or equivalently in terms of the local Damköhler number at the flame edge, as predicted by theory. Naturally, the effects of unsteadiness in this flow produce a broad joint p.d.f. The statistics collected also suggest that the mean value of the hydrogen radical reaction rate are very small in the turbulent regions of the flow owing to the functional form of the hydrogen radical reaction rate itself. The consequence of these results in the context of turbulent combustion modelling is discussed. Additional statistical and morphological information of the flame is provided.

1. Introduction

Extinction dynamics in turbulent diffusion flames remains an open and challenging subject. It is known that when a diffusion flame encounters a sufficiently large rate of strain (equivalent to the rate of scalar dissipation) the flame can extinguish owing to an imbalance of chemical heat production to diffusion from the flame (Peters 1986). The extinguished region and the burning flame are separated by a flame edge with a strain-rate-dependent structure (Vervisch & Poinsot 1998). This extinction front can expand or collapse depending on the dynamics of the flow, transport properties and the chemistry details. Flame surface can also be produced under certain conditions that are generally referred to as turbulent reignition. Two mechanisms are thought to be responsible for flame creation. In one mechanism, flame edges that separate the burning from the quenched regions, propagate against the flow and they are able to

heal or close the extinguished region. In the other mechanism, reignition can take place when hot pockets of reacted products and mixed non-burning reactants are brought into contact, through convection and diffusion, for a sufficient amount of time. Hot pockets of products are left-overs from the pre-quenched state or can be convected from nearby burning flame sections. Mixing of reactants takes place through diffusion in the post-quenched region. In jet diffusion flames close to extinction, this mechanism may not play a significant role in the near-field region of the jet, where the rate of strain is largest, if both streams are cold because the ignition delay time of typical hydrocarbon mixtures at low temperatures is too large in comparison with the characteristic flow time. Only the first mechanism seems dominant. On the other hand, further downstream of the jet, the level of turbulence may be sufficiently strong to quench the flame locally and reignition through the second mechanism could take place. These two mechanisms for flame creation together with the extinction mechanism due to large rate of strain are considered to be dominant in flame extinction reignition dynamics.

The study of edge-flame dynamics is relatively well advanced, at least in one- and two-dimensional configurations (including axisymmetric). The first experimental evidence is due to Phillips (1965) and theoretical results date back to Liñán & Crespo (1976), Dold (1988) and Buckmaster & Matalon (1988). Buckmaster (2002) reviewed the current understanding of the dynamics of flame edges. In general, the flame edges are composed of two premixed branches, a rich and a lean branch, and a diffusion flame aligned with the stoichiometric line in what is called colloquially a triple flame. For large values of the strain rate, the two premixed branches merge into a single edge. In all these cases, there is a well-defined edge propagation velocity, referred to here as the edge-flame velocity, that depends on the Damköhler number (the flow to chemistry time scale ratio), the Lewis number (the thermal to molecular diffusivity ratio) (Buckmaster 1996, 2001) and the level of heat release. This velocity can be negative if the rate of strain is sufficiently large. Theoretical descriptions of triple edge-flames using the large activation energy asymptotic approximation with zero heat release (Daou & Liñán 1998) and with finite heat release (Ghosal & Vervisch 2000) have been developed. Detailed numerical studies have also been carried out for freely propagating edge-flames without the effects of heat release by Kioni *et al.* (1993) and with the effects of heat release by Ruetsch, Vervisch & Liñán (1995) and Echekki & Chen (1998). In the interest of understanding the interaction of the flame edges in more complex flows, some studies have considered the interaction of the edge-flame with a counterflow that is perpendicular to the plane of the flame, also called a strained mixing layer (Daou & Liñán 1998; Vedarajan & Buckmaster 1998; Buckmaster & Short 1999; Thatcher & Dold 2000; Short, Buckmaster & Kochevets 2001). Experiments have also been performed. Shay & Ronney (1998) studied the effects of variable strain rate in space and showed the formation of stable edge-flames. In the case of triple-edge flames, Ko & Chung (1999) performed experiments with methane–air jets and report that their unsteady edge flames propagate at a speed that increases with decreasing mixture fraction gradient, in agreement with theoretical predictions. Santoro, Liñán & Gomez (2000) have performed experimental measurements of methane–air flames in a counterflow mixing layer and find the existence of standing edge-flames, with triple-flames for large Damköhler number and simple edge-flames for lower Damköhler numbers.

In the case of three-dimensional turbulent flows, most studies have been carried out with the aid of experimental diagnostic techniques (Everest *et al.* 1995; Kelman & Masri 1997; Muñiz & Mungal 1997, 2001; Stårner *et al.* 1997; Barlow & Frank 1998; Rehm & Clemens 1999; Meier *et al.* 2000; Dally, Karpetis & Barlow 2002; Karpetis &

Barlow 2002). Several studies have documented the formation of extinction pockets in diffusion flames, see Everest *et al.* (1995) and Kelman & Masri (1997) among others. The most detailed experimental data corresponds to planar cuts of the physical domain of interest and the three-dimensional structure of the flame is not examined. For this reason, numerical simulation can aid in the pursuit of a better understanding of extinction dynamics. Unfortunately, the computational turbulent combustion community faces a large disparity between available computational resources and the requirements of fully turbulent reacting flows involving realistic chemistry. The majority of detailed chemistry simulations are only accessible in two dimensions, even in the largest supercomputers. Only recently has numerical simulation become sufficiently powerful to attack three-dimensional flows. Here, we understand numerical simulations as direct numerical simulation (DNS) in which all temporal and spatial scales of the flow and the chosen chemistry are accurately resolved. In their review of DNS of non-premixed turbulent combustion Vervisch & Poinsot (1998) identified four different types of relevant analysis. The first three types of analysis identified by Vervisch & Poinsot (1998) have been investigated in the past, see Pantano, Sarkar & Williams (2003 and references therein) for the case of typical heat release in a methane–air shear layer. The present paper is centred around the fourth type of analysis, concerning effects of finite-rate chemistry. In the present study, we concentrate on scalar fields that are active, that is, they affect pressure, density or velocity fields. The coupling takes place through variations of the density owing to heat release and owing to the presence of non-zero chemical source terms of finite or infinite rate (reactive fields). DNS of active reactive scalars has been discussed in reviews (Jou & Riley 1989; Givi 1989; Vervisch & Poinsot 1998). The flow configurations considered range from homogeneous isotropic turbulence (Mell *et al.* 1994; Mahalingam, Chen & Vervisch 1995; Swaminathan, Mahalingam & Kerr 1996; Montgomery, Kosály & Riley 1997; Swaminathan & Bilger 1997; Bédat, Egolfopoulos & Poinsot 1999; Livescu, Jaberi & Madnia 2002), temporally evolving turbulent shear layers (McMurtry, Riley & Metcalfe 1989; Miller, Madnia & Givi 1994; Pantano *et al.* 2003), spatially evolving grid turbulence (Cook & Riley 1996) and jets (Mizobuchi *et al.* 2002). Of all these works, that of Mizobuchi *et al.* (2002) is the most relevant in our context. They performed a simulation of a three-dimensional lifted hydrogen flame issuing from a square duct and used a detailed chemical mechanism of hydrogen–oxygen combustion. In their case, owing to the very short reaction times characteristic of hydrogen combustion, no flame holes were observed.

With our current computational resources, the most promising chemistry models that can be incorporated in three-dimensional simulations of turbulent combustion are restricted to reduced chemical mechanisms. Past works include Swaminathan & Bilger (1997), who investigated a model two-step chemical mechanism for methane–air combustion and Montgomery *et al.* (1997) who used a three-step reduced mechanism to simulate hydrogen–oxygen non-premixed combustion. Bédat *et al.* (1999) used an integrated combustion chemistry (ICC) methodology in which the chemical scheme is postulated and the parameters of the scheme are determined by matching several flame properties. In the present study, we are interested in methane–air combustion and we chose a chemical mechanism that is sufficiently complex to include as many details of the chemical structure of the flame as possible while being computationally tractable. This mechanism is the four-step reduced mechanism of Peters (1985) and was selected for several reasons. First, it is shown by Peters (1985) that the mechanism is deduced systematically from a skeletal C-1 mechanism assuming steady-state approximations of some radicals and partial equilibrium for some reactions. Thus, there is some

degree of connection with the more complete chemistry (the mechanism is not ad hoc). Secondly, it has been shown by Peters (1985) that predictions of extinction strain rate resulting from this reduced mechanism are in good agreement with those obtained using the full mechanism and that the internal structure of the flame is reproduced well both qualitatively and quantitatively for most species. Thirdly, extensive studies of the asymptotic structure of the flame using the reduced mechanism are available (Seshadri & Peters 1988; Bai & Seshadri 1999). In these studies, rate-ratio asymptotics is used to understand the internal structure of the flame. It is known that the flame is composed of the classical external Burke–Schumann structure. The inner structure is composed of a thin $H_2 - CO$ oxidation layer of thickness $O(\epsilon)$ towards the lean side, a thin water gas shift non-equilibrium reaction of thickness $O(\nu)$ and a thin fuel consumption layer towards the fuel side of thickness $O(\delta)$. Analysis of the inner structure for large values of the Damköhler number shows that $\epsilon > \nu > \delta$. There is even some work on the inner structure of methane–oxygen–nitrogen diffusion flames (Chelliah & Williams 1990). Lastly, the mechanism has been successfully used by several authors in one- and two-dimensional flows (see Peters & Kee 1987; Card *et al.* 1994; James & Jaberi 2000).

The objective of the present study is to investigate the behaviour of flame edges with complex chemistry in three-dimensional flows. The present work addresses realistic heat release and requires the computations of 8 scalar species employing as many as 100 million grid points. A fully compressible code, similar to that used in Pantano *et al.* (2003), is employed, with a convective Mach number (Bogdanoff 1983; Papamoschou & Roshko 1988), defined as $M_c = \Delta u/(c_1 + c_2)$ (where Δu is the velocity difference between the coflow and the jet, and c_1 and c_2 are the speeds of sound of each stream), equal to 0.3. This value is small enough that compressibility effects from Mach number are not important (Pantano *et al.* 2003). For future reference, we introduce the concept of mixture fraction and scalar dissipation. A common approach in the modelling of non-premixed turbulent combustion is based on knowledge of two variables; a mixture fraction, Z, that represents the mixture composition, giving the fraction of the material that comes from the fuel stream, and its so-called scalar dissipation, $\chi = 2D\nabla Z \cdot \nabla Z$ (in which D is its molecular diffusivity), χ being related to the rate of dissipation of fluctuations of Z in turbulent flow (see Williams 1985). These two quantities are used in the analysis of the results described in § 6.

2. The flow configuration

Figure 1 is a sketch of the planar jet (a model of a slot burner) considered here. The jet velocity is U_j, the coflow velocity is U_c and the velocity difference is $\Delta u = U_j - U_c$. The domain size is L_1 in the streamwise direction, L_2 in the transverse direction and L_3 in the spanwise direction. The jet height is denoted by H. The jet is composed of a mixture of methane and nitrogen. The coflow is composed of air approximated as a mixture of oxygen and nitrogen. Both, methane and oxygen, mass fractions are equal to 0.23. These values were chosen because the global chemistry that occurs at the flame,

$$CH_4 + 2O_2 \rightarrow CO_2 + 2H_2O, \tag{2.1}$$

then yields a stoichiometric mixture fraction $Z_s = 0.2$. A more complete argument regarding our choice of stoichiometry can be found in Pantano *et al.* (2003).

In order to reduce the computational cost associated with full chemistry models, the reduced mechanism of Peters (1985) for combustion of methane was chosen in

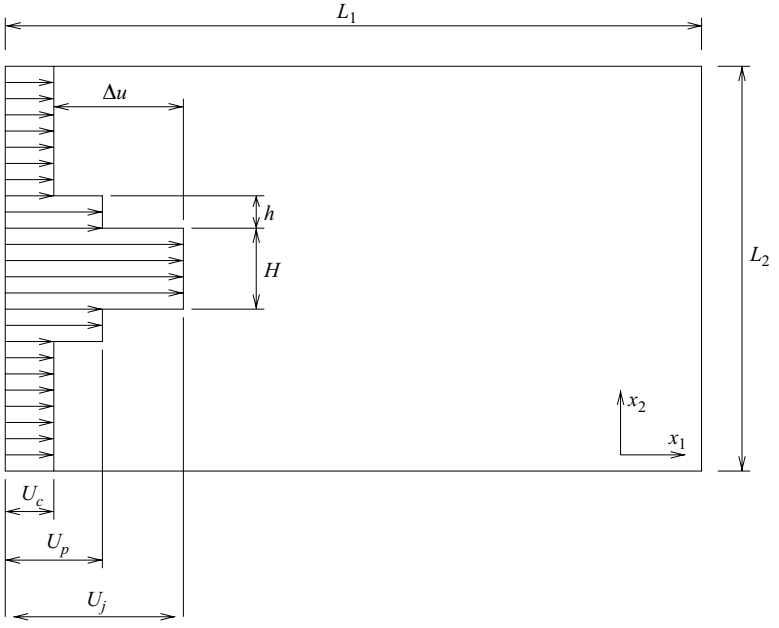

FIGURE 1. Schematic diagram of the spatially evolving jet with streamwise velocity profile parameters shown in a two-dimensional projection ($x = x_1$, $y = x_2$, $z = x_3$).

this study. In this four-step mechanism, derived from a skeletal C-1 mechanism by systematic application of quasi-steady state and partial equilibrium approximations, the resulting non-linear relationships between the mass fractions of the species in quasi-steady state are truncated. This renders the algebraic expressions of the reaction rates explicit. The mechanism involves $N = 8$ species, namely, CH_4, O_2, H_2O, CO_2, CO, H_2, H and N_2. Thus, seven transport equations with non-zero reaction rates must be solved along with the flow variables. The mass fraction of N_2 is obtained from the balance of all species and no transport equation is thus required for this inert species. The reaction-rate expressions for the rates of production–consumption of species are provided as algebraic expressions of the concentrations and temperature in Seshadri & Peters (1988).

To make the influence of density variation exclusively associated with heat release, the jet and coflow have the same density. To also make their pressures equal requires a temperature ratio equal to the average molecular weight ratio of the air in the coflow to that of the fuel in the jet (ideal gas at low Mach number). Thus, the air temperature is 20% higher than the fuel temperature of 298 K. Specific heats of the species in the ideal gas mixture are allowed to depend on temperature, to maintain correct cold-gas values and avoid achieving flame temperatures that are too high at the reaction sheet, which would result in unrealistically low gas densities. The specific heats at constant pressure and enthalpy were obtained from NASA polynomial fits (McBride, Gordon & Reno 1993). The values of these parameters give an adiabatic flame temperature for $Z_s = 0.2$ of $T_f = 2022$ K.

To clarify interpretations by focusing attention on as few different physical phenomena as possible, simplifications were introduced in molecular transport properties. The viscosity μ was taken to be proportional to T^m. All chemical species were assumed to have diffusion coefficient, D_i, that have the same temperature dependence, namely,

CH_4	O_2	H_2O	CO_2	CO	H_2	H	N_2
0.97	1.11	0.83	1.39	1.10	0.30	0.18	1.00

TABLE 1. Constant Lewis number of involved species used in the simulation (Smooke & Giovangigli 1991).

ρD_i is proportional to T^m so that the Schmidt number, $Sc_i = \mu/\rho D_i$, is constant. Also imposed is constancy of the Prandtl number, $Pr = \mu C_p/\kappa$, where κ denotes the thermal conductivity. Because of the variations of the specific heat C_p of the mixture, κ also varies to maintain Pr constant. The approximate value for air, $Pr = 0.7$, is employed throughout. The reference values of D_i at T_o were obtained from Smooke & Giovangigli (1991) and were such that the Schmidt number is constant and equal to the product of the Prandtl number times the Lewis number, $Sc_i = Pr\, Le_i$, where $Le_i = \kappa/(C_p \rho D_i)$. The values of the Lewis numbers of the different species are specified in table 1. The effects of differential diffusion are thereby taken into account in this simplified transport model.

To enhance flame stability at the inflow and avoid flame lift-off or blow-out, a pilot is inserted between the jet core and the main coflow. This pilot is implemented numerically as a thin coflow with a high temperature, equal to the adiabatic flame temperature of the jet–coflow mixture stoichiometry. Moreover, the pilot streamwise velocity is slightly higher than that of the main coflow to avoid recirculation. This technique has been used by Wall, Boersma & Moin (2000) to stabilize round jet flames. The flame at this pilot conditions burns below the quenching scalar rate of dissipation and remains attached to the inflow of the domain.

3. Formulation

The unsteady three-dimensional compressible Navier–Stokes equations for a Newtonian fluid composed of a reacting ideal-gas mixture are considered in this study. Energy conservation is written as a pressure equation to facilitate computation. Relevant parameters are the Reynolds number,

$$Re = \frac{\rho_o \Delta u H}{\mu_o}, \tag{3.1}$$

the non-dimensional heat release,

$$Q = \frac{q_o Y_{F,f} Z_s}{C_{pN_o} T_o \nu_F W_F}, \tag{3.2}$$

and the Damköhler number,

$$Da = \frac{t_o W_O A_o}{\rho_o}. \tag{3.3}$$

In (3.1), μ_o is the viscosity of the mixture at T_o and in (3.2), q_o denotes the enthalpy of the reaction, (2.1), Williams (1985),

$$q_o = \sum_{i=1}^{N} \nu_i W_i \Delta h_i^o. \tag{3.4}$$

The enthalpy of formation of species i is denoted by Δh_i^o, W_i is the molecular weight of species i, $\nu_{CH_4} = \nu_F = 1$, $\nu_{O_2} = \nu_O = 2$, $\nu_{CO_2} = -1$, $\nu_{H_2O} = -2$ and C_{pN_o} is the specific

heat of nitrogen at T_o. The molecular weights, W_i, are dimensional quantities in this paper (units of gram per mol). The reference molecular weight is that of oxygen, O_2, and is denoted by W_O. In (3.3), A_o is a characteristic reaction rate (units of moles per unit volume and time) and is specified below in terms of one of the reaction rates of the chemical mechanism. The choice of characteristic chemical time is not unique for a multistep mechanism and it is discussed in § 3.2. The formulation is non-dimensional, the unit length being H, velocity Δu, time $t_o = H/\Delta u$, density ρ_o, temperature T_o, enthalpy $C_{pO_o} T_o$ and pressure $\rho_o \Delta u^2$. The inert mass fraction, N_2, is determined from

$$Y_{N_2} = 1 - \sum_{i \neq N_2} Y_i. \tag{3.5}$$

Here, the subscripts O and F stand for oxidizer, O_2, and fuel, CH_4, respectively, and $Y_{O,o}$ is the mass fraction of oxygen in the oxidizer (air) stream, while $Y_{F,f}$ is the mass fraction of fuel (methane) in the fuel stream. The stoichiometric mixture fraction, Z_s, is equal to

$$Z_s = \frac{1}{\phi + 1}, \tag{3.6}$$

where $\phi = (W_O \nu_O Y_{F,f})/(W_F \nu_F Y_{O,o})$ is the fuel–air equivalence ratio. The Mach number is $M = \Delta u / \sqrt{\gamma_o R_o T_o}$, γ_o and R_o being the ratio of specific heats and gas constant for O_2 at T_o, and the normalized average molecular weight is

$$\overline{W} = \left(W_O \sum_{i=1}^{N} \frac{Y_i}{W_i} \right)^{-1}. \tag{3.7}$$

3.1. *Governing equations*

The conservation equation for species mass fractions, Y_i, is

$$\frac{\partial(\rho Y_i)}{\partial t} + \frac{\partial(\rho Y_i u_k)}{\partial x_k} = \frac{1}{Re\, Sc_i} \frac{\partial}{\partial x_k} \left(\delta^* \frac{\partial Y_i}{\partial x_k} \right) + Da\ \dot{\omega}_i, \tag{3.8}$$

where the reaction rate term $\dot{\omega}_i$ is given in § 3.2 for each species. The conservation equations for mass, momentum and energy are

$$\frac{\partial \rho}{\partial t} + \frac{\partial(\rho u_k)}{\partial x_k} = 0, \tag{3.9}$$

$$\frac{\partial(\rho u_i)}{\partial t} + \frac{\partial(\rho u_k u_i)}{\partial x_k} = -\frac{\partial p}{\partial x_i} + \frac{\partial \sigma_{ik}}{\partial x_k}, \tag{3.10}$$

and

$$\begin{aligned} \frac{\partial p}{\partial t} + u_k \frac{\partial p}{\partial x_k} = & -\gamma p \frac{\partial u_k}{\partial x_k} + \frac{(\gamma - 1)}{(\gamma_o - 1) Re\, Pr M^2} \frac{\partial}{\partial x_k} \left(\kappa^* \bar{C}_p \frac{\partial T}{\partial x_k} \right) \\ & + (\gamma - 1) \Phi + \frac{(\gamma - 1)}{(\gamma_o - 1) Re M^2} \sum_{i=1}^{N-1} \frac{C_{pi} - C_{pN}}{Sc_i} \delta^* \frac{\partial T}{\partial x_k} \frac{\partial Y_i}{\partial x_k} \\ & + \frac{\gamma T}{\gamma_o Re M^2} \sum_{i=1}^{N-1} \left(\frac{1}{W_i} - \frac{1}{W_N} \right) \frac{W_O}{Sc_i} \frac{\partial}{\partial x_k} \left(\delta^* \frac{\partial Y_i}{\partial x_k} \right) \\ & + \frac{Da}{M^2} \sum_{i=1}^{N-1} \left(\frac{\gamma}{\gamma_o} \frac{W_O}{W_i} T - \frac{\gamma - 1}{\gamma_o - 1} h_i \right) \dot{\omega}_i. \end{aligned} \tag{3.11}$$

In (3.10), the viscous stress tensor is given by

$$\sigma_{ij} = \frac{\mu^*}{Re}\left\{\frac{\partial u_i}{\partial x_j} + \frac{\partial u_j}{\partial x_i} - \frac{2}{3}\frac{\partial u_k}{\partial x_k}\delta_{ij}\right\}, \tag{3.12}$$

and in (3.11), the viscous dissipation is

$$\Phi = \sigma_{ij}\frac{\partial u_i}{\partial x_j}. \tag{3.13}$$

The non-dimensional average specific heat of the mixture is

$$\bar{C}_p = \sum_{i=1}^{N} C_{pi}(T) Y_i, \tag{3.14}$$

where the specific heats at constant pressure, $C_{pi}(T)$ are expressed as polynomial functions of the temperature with coefficients given by McBride *et al.* (1993). The enthalpy, h_i, is defined by

$$h_i = \frac{\Delta h_i^o}{C_{pO_o} T_o} + \int_1^T C_{pi}(T)\,\mathrm{d}T. \tag{3.15}$$

The non-dimensional equation of state of the mixture is

$$p = \frac{\rho T}{\gamma_o M^2 \overline{W}}. \tag{3.16}$$

The specific heat ratio of the mixture, γ, varies somewhat and is given by

$$\gamma = \frac{\gamma_o}{\gamma_o - (\gamma_o - 1)/\overline{W}\bar{C}_p}. \tag{3.17}$$

The non-dimensional transport coefficients μ^*, δ^* and κ^* are given by

$$\mu^* = \delta^* = \kappa^* = T^m, \tag{3.18}$$

with $m = 0.7$. The heat-release parameter Q of (3.2) is equal to 7.45 and it would be equal to $T_f/T_o - 1$ if the specific heat of the mixture were constant.

Finally, a mixture fraction field, Z, is computed along with the rest of the variables. This field obeys the following transport equation,

$$\frac{\partial(\rho Z)}{\partial t} + \frac{\partial(\rho Z u_k)}{\partial x_k} = \frac{1}{Re\,Sc}\frac{\partial}{\partial x_k}\left(\delta^*\frac{\partial Z}{\partial x_k}\right), \tag{3.19}$$

where the mixture fraction Schmidt number is $Sc = Pr$. This implies that the Lewis number is one for this field. The Z field is used to initialize the flame and to help in the interpretation and extraction of statistical information.

3.2. *Chemistry model*

Peters (1985) reduced mechanism can be represented by the following global reactions

$$\begin{aligned} CH_4 + 2H + H_2O &= CO + 4H_2 \qquad (I),\\ CO + H_2O &= CO_2 + H_2 \qquad (II),\\ H + H + M &= H_2 + M \qquad (III),\\ O_2 + 3H_2 &= 2H + 2H_2O \qquad (IV), \end{aligned}$$

Reaction	$\hat{A}_i$	β_i	E_i
k_1	1.2×10^{17}	−0.91	69.10
k_5	2.0×10^{18}	−0.8	0.0
k_{10}	1.656×10^{7}	1.5247	60.042
k_{11}	2.2×10^{4}	3.0	36.6

TABLE 2. Specific dimensional reaction-rate parameters. Units in cm, mole, Kelvin and kJ.

with corresponding non-dimensional reaction rates given by

$$\dot{\omega}_I = k_{11} C_{\mathrm{CH_4}} C_{\mathrm{H}}, \tag{3.20}$$

$$\dot{\omega}_{II} = k_{10} \left(C_{\mathrm{H}} / C_{\mathrm{H_2}} \right) \left(C_{\mathrm{CO}} C_{\mathrm{H_2O}} - C_{\mathrm{CO_2}} C_{\mathrm{H_2}} / K_{II} \right), \tag{3.21}$$

$$\dot{\omega}_{III} = k_5 C_{\mathrm{O_2}} C_{\mathrm{H}} C_M, \tag{3.22}$$

$$\dot{\omega}_{IV} = k_1 C_{\mathrm{H}} \left(C_{\mathrm{O_2}} - C_{\mathrm{H}}^2 C_{\mathrm{H_2O}}^2 / C_{\mathrm{H_2}}^3 K_{IV} \right). \tag{3.23}$$

The non-dimensional concentrations, C_i, are defined as

$$C_i = \frac{\rho Y_i W_O}{W_i}, \tag{3.24}$$

and the third body concentration, C_M, is defined as

$$C_M = \sum_{i=1}^{N} \eta_i C_i, \tag{3.25}$$

with catalytic efficiencies $\eta_{\mathrm{CH_4}} = \eta_{\mathrm{H_2O}} = 6.5$, $\eta_{\mathrm{O_2}} = \eta_{\mathrm{N_2}} = 0.4$, $\eta_{\mathrm{CO_2}} = 1.5$, $\eta_{\mathrm{CO}} = 0.75$ and $\eta_{\mathrm{H_2}} = \eta_{\mathrm{H}} = 1$ (Smooke & Giovangigli 1991). The mechanism given by (I)–(IV) is a global representation of the chemistry and should not be confused with the actual paths that the reaction takes. These are not elementary reactions; their rates are expressed as algebraic functions of rates appearing in the skeletal C-1 mechanism. These reaction-rate constants are given in the customary Arrhenius form,

$$k_i = A_i T^{\beta_i} \mathrm{e}^{-T_i/T}, \tag{3.26}$$

where $T_i = E_i / R$ with R the universal gas constant, equal to $8.314\,\mathrm{J\,mol^{-1}\,K^{-1}}$ and E_i is the activation energy of the elementary reaction i. In (3.20) to (3.26), all parameters are non-dimensional. The remaining constants, K_{II} and K_{IV}, are

$$K_{II} = 3.9512\ 10^{-3}\ T^{0.8139}\, \mathrm{e}^{16.6247/T}, \tag{3.27}$$

$$K_{IV} = 2.7405\ T^{-0.2484}\, \mathrm{e}^{19.262/T}. \tag{3.28}$$

The values of the parameters appearing in (3.26) were obtained by non-dimensionalizing the dimensional rate constants reported in Seshadri & Peters (1988) and shown in table 2 by the largest of the rates at T_o, in this case, that of reaction k_5. This dimensional rate is given by

$$A_o = \hat{A}_5 T_o^{\beta_5}\, \mathrm{e}^{-E_5/RT_o} \left(\frac{\rho_o}{W_O} \right)^3, \tag{3.29}$$

and was used in (3.3) to define the Damköhler number.

The reaction rates, $\dot{\omega}_i$, appearing in (3.8) are defined in terms of (3.20)–(3.23) by

$$\dot{\omega}_{\mathrm{CH_4}} = -\frac{W_{\mathrm{CH_4}}}{W_O}\dot{\omega}_I, \tag{3.30}$$

$$\dot{\omega}_{\mathrm{O_2}} = -\frac{W_{\mathrm{O_2}}}{W_O}\dot{\omega}_{IV}, \tag{3.31}$$

$$\dot{\omega}_{\mathrm{H_2O}} = \frac{W_{\mathrm{H_2O}}}{W_O}(2\dot{\omega}_{IV} - \dot{\omega}_{II} - \dot{\omega}_I), \tag{3.32}$$

$$\dot{\omega}_{\mathrm{CO_2}} = \frac{W_{\mathrm{CO_2}}}{W_O}\dot{\omega}_{II}, \tag{3.33}$$

$$\dot{\omega}_{\mathrm{CO}} = \frac{W_{\mathrm{CO}}}{W_O}(\dot{\omega}_I - \dot{\omega}_{II}), \tag{3.34}$$

$$\dot{\omega}_{\mathrm{H_2}} = \frac{W_{\mathrm{H_2}}}{W_O}(4\dot{\omega}_I + \dot{\omega}_{II} + \dot{\omega}_{III} - 3\dot{\omega}_{IV}), \tag{3.35}$$

$$\dot{\omega}_{\mathrm{H}} = 2\frac{W_{\mathrm{H}}}{W_O}(\dot{\omega}_{IV} - \dot{\omega}_I - \dot{\omega}_{III}). \tag{3.36}$$

A common difficulty encountered in the implementation of reduced mechanisms, as the one considered here, is the presence of algebraic terms in the denominator of the reaction-rate expressions. When the denominator goes to zero, the reaction rate becomes infinitely large. In our case, the presence of the concentration of H_2 in the denominator of (3.21) and (3.23) leads to this undesired behaviour. In regions where there is no H_2, these expressions diverge to infinity and an appropriate regularization must be applied for numerical purposes. As suggested by Peters (1991), a common regularization is to add a small constant, ϵ_o, to the denominator of (3.21) and (3.23) so that $1/C_{\mathrm{H_2}}$ becomes $1/(C_{\mathrm{H_2}}+\epsilon_o)$, in order to avoid the singularity. This regularization was sufficient in a one-dimensional flamelet test calculation. Unfortunately, in our simulation, it was found that shifting the hydrogen concentration by ϵ_o was not satisfactory at all points of the domain. We could still find very compact regions with unphysically high values of the reaction rates far away from the flame. After some trial and error, it was decided to regularize the algebraic singularity in hydrogen concentration with

$$\frac{1}{C_{\mathrm{H_2}}} \rightarrow \begin{cases} 0, & 0 \leqslant C_{\mathrm{H_2}} < \epsilon_o, \\ \tanh\left(\dfrac{C_{\mathrm{H_2}} - \epsilon_o}{\epsilon_o}\right)\dfrac{1}{3\epsilon_o}, & \epsilon_o \leqslant C_{\mathrm{H_2}} < 3\epsilon_o, \\ \dfrac{1}{C_{\mathrm{H_2}}}, & 3\epsilon_o \leqslant C_{\mathrm{H_2}}. \end{cases} \tag{3.37}$$

Here, the value of ϵ_o was chosen to be approximately equal to 1% of the maximum concentration of H_2 in the simulation, namely, $\epsilon_o = 1.6 \times 10^{-5}$. These choices allowed a very smooth transition of the reaction rates from the flame region to the regions where $C_{\mathrm{H_2}}$ was zero.

3.3. *Numerical scheme, flow initialization and boundary conditions*

The simulation proceeds in the following way: suppose that the variables ρ, p, u_i and Y_i are available at a given time. The temperature is obtained from (3.16) after using (3.7). The enthalpy and specific heat are then computed from (3.14)–(3.15). Finally,

(3.8)–(3.11) are solved using a semi-implicit time integration to advance the variables in time.

In direct simulation of multi-species turbulent reactive flows close to flame extinction, the flow and chemical time scales are comparable, but the spatial resolution required for chemistry demands fine grids in order to resolve the thin reaction zones. Furthermore, some of the chemical species can be very diffusive, in our case, these species are hydrogen and hydrogen radical (see table 1). The time step allowed when integrating the governing equations with explicit schemes is controlled by the diffusive stability limit dictated by these few chemical species. We overcome this problem by integrating implicitly the diffusive terms of the hydrogen and hydrogen radical governing equations, while all other terms are integrated explicitly. In our case, we use a third-order additive semi-implicit Runge–Kutta scheme (Pantano 2004).

Spatial derivatives are computed using a compact Padé scheme in space of sixth-order of accuracy (Lele 1992). Characteristic inflow boundary conditions are imposed in the streamwise direction, x_1, and 'non-reflective' boundary conditions are imposed in the x_2-direction (Baum, Poinsot & Thévenin 1995; Stanley, Sarkar & Mellado 2002). The grid was uniform in the x_1- and x_3-directions with an equal grid spacing, Δx, in both directions. In the transverse direction, x_2, the grid is uniform across the centre of the domain enclosing the thickness of the jet and it is stretched gradually in the rest of the domain. The grid spacing in the centre of the domain in the transverse direction is also Δx, while the stretching was 1% in the corresponding part of the domain.

The flow is initialized to a hyperbolic-tangent profile for the mean streamwise velocity, $\bar{u}_1(x_2)$,

$$\bar{u}_1(x_2) = \begin{cases} \dfrac{U_j + U_p}{2} + \dfrac{U_j - U_p}{2} \tanh\left(-\dfrac{(x_2 - H/2)}{2\delta_o}\right), & x_2 < \dfrac{H+h}{2}, \\ \dfrac{U_p + U_c}{2} + \dfrac{U_p - U_c}{2} \tanh\left(-\dfrac{(x_2 - H/2 - h/2)}{2\delta_o}\right), & x_2 > \dfrac{H+h}{2}, \end{cases} \tag{3.38}$$

while the transverse mean velocity components are set to zero. The symmetric part of the jet is initialized by mirroring the solution with respect to the symmetry axis. The coflow velocity is denoted by U_c, the jet velocity by $U_j = U_c + \Delta u$ and the pilot velocity is denoted by U_p. The value of $\delta_o = 0.05H$ is employed in the simulation. The mean pressure is set initially to a uniform value and $\rho_j = \rho_c = 1$ throughout, where ρ_j is the jet density and ρ_c is the density of the coflow stream. In addition to the mean fields, broadband fluctuations are used to accelerate the transition to turbulence. This is achieved by generating a random velocity field with an isotropic turbulence spectrum of the form

$$E(k) = (k/k_o)^4 \exp(-2(k/k_o)^2), \tag{3.39}$$

where k is the wavenumber and k_o the wavenumber of peak energy. The extent of the initial velocity fluctuations is limited in the cross-stream direction by an exponential decay given by,

$$\exp(-((x_2 \pm H/2)/\delta_b)^2), \tag{3.40}$$

where $\delta_b = \delta_o$. The initial pressure fluctuations are obtained from the Poisson equation for incompressible flow.

The species mass fraction were initialized in a two-stage process. First, a passive scalar, Z, representing a mixture fraction variable was initialized to

$$\bar{Z}(x_2) = \begin{cases} \dfrac{1+Z_s}{2} + \dfrac{1-Z_s}{2}\tanh\left(-\dfrac{(x_2 - H/2)}{2\delta_o}\right), & x_2 < \dfrac{H+h}{2}, \\ \dfrac{Z_s}{2} + \dfrac{Z_s}{2}\tanh\left(-\dfrac{(x_2 - H/2 - h/2)}{2\delta_o}\right), & x_2 > \dfrac{H+h}{2}, \end{cases} \tag{3.41}$$

with initial scalar fluctuations set to zero. The temperature and density were set to the Burke–Schumann values, $T^e(Z)$ and $\rho^e(Z)$ (Williams 1985), respectively. The simulation was run for a number of time steps, of the order of two flow transient times, based on the jet exit velocity, L_x/U_j, until the jet instability modes develop and the unphysical initial conditions are washed out of the domain. Secondly, a one-dimensional flamelet calculation was carried out to obtain $Y_i^e(Z)$. The flamelet solution was obtained from the steady flamelet equation of Peters (1984),

$$-\frac{\rho\chi}{2Le_i}\frac{\mathrm{d}^2 Y_i^e}{\mathrm{d}Z^2} = Da\,\dot{\omega}_i(Y^e, T), \tag{3.42}$$

with the scalar dissipation given by $\chi = 8Z_s/Re\delta_o^2$. Solution of the boundary-value problem, (3.42), gives the mass fraction of all species and temperature as a function of Z. The species mass fractions were then initialized through the mapping $Y_i = Y_i^e(Z)$, where Z was the result of the previous initialization step. Prescription of the initial scalar field gives initial distributions of Y_i and $\overline{W}$ from previous equations.

The computational domain is composed of two parts. A so-called inflow domain that contains streamwise periodic flow that is convected into the primary larger domain. This technique is described, for example, by Li, Balaras & Piomelli (2000) and by Stanley *et al.* (2002) for planar spatially evolving jets. The data contained in the inflow domain are obtained by performing a temporal simulation (with periodic streamwise boundary conditions) for a short but otherwise sufficient time to allow the desired level of inflow fluctuations to be injected in the primary domain. The temporal simulation data at one instant in time (frozen flow) is then convected at constant speed, $(U_j + U_c)/2$, using Taylor's hypothesis to relate spatial to temporal derivatives; required by the incoming characteristic boundary conditions of the spatial simulation. The peak turbulence intensity level of the inflow forcing is around 4%.

Since the kinematic viscosity increases with temperature, the Reynolds number, Re, was deliberately kept large at 3000. The Mach number that appears in (3.11) was set to $M = 0.694$ and the Damköhler number was set to $Da = 5000$. The composition of the coflow and the jet is $Y_{O,o} = 0.23$ and $Y_{F,f} = 0.23$ and gives a stoichiometric mixture fraction value of $Z_s = 0.2$. The Prandtl number is 0.7. The main coflow velocity, $U_c/\Delta u$ is 0.03, the pilot velocity, $U_p/\Delta u$ is 0.3 and the pilot width, h/H, is 0.325. If we assume atmospheric pressure and the viscosity of air at 298 K, H is approximately equal to 2 mm for the values of Reynolds and Damköhler numbers of this simulation. This jet height is similar to the jet diameter used by Mizobuchi *et al.* (2002) in a simulation of a hydrogen–air lifted jet. The number of grid points was $N_x = 1024$ in the streamwise direction, $N_y = 512$ in the transverse direction and $N_z = 192$ in the spanwise direction. The total number of grid points is roughly 100 million and there were 13 variables that had to be integrated, five fluid mechanical and 8 scalars. The large resolution requirements were mandated by the need to resolve the fuel consumption layer of the methane–air mechanism (Seshadri & Peters 1988). It is well known that this region must be well resolved in order to avoid numerical extinction of the flame owing to lack

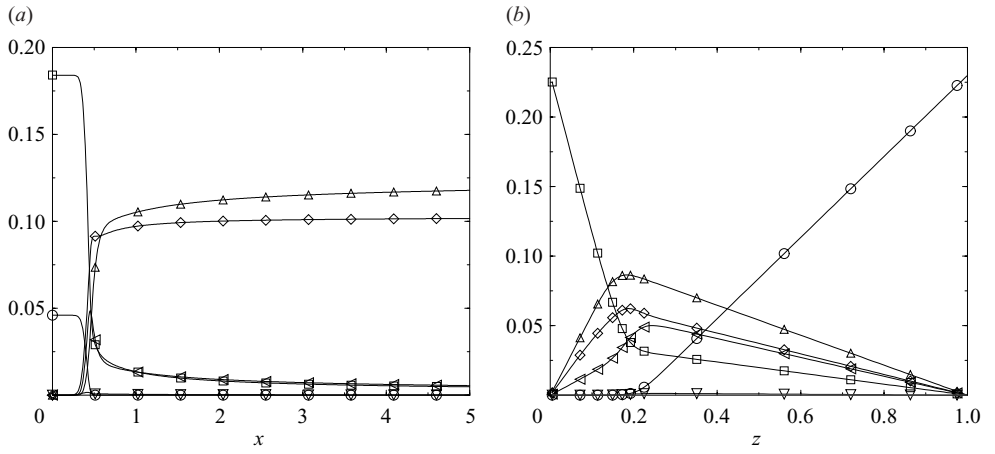

FIGURE 2. Mass fraction profiles: (*a*) premixed flame as a function of distance and (*b*) flamelet solution close to extinction as a function of mixture fraction. ○, CH_4; □, O_2; ◇, H_2O; △, CO_2; ◁, CO; ▽, H_2.

of resolution. In our case, a resolution of approximately 10 points across the fuel consumption layer was found to be sufficient with our numerical scheme (Vervisch & Poinsot 1998). The analogous flow with single-step or infinitely fast chemistry can typically be resolved with at least half the resolution in each direction. For a three-dimensional flow, this implies a cost reduction in space of approximately an order of magnitude. As pointed out in Swaminathan & Bilger (1997), the simplifications involved in deriving the reduced mechanism of Peters lead to an excessively thin fuel consumption zone, while maintaining good extinction characteristics. It is possible to artificially alter the rates of the fuel consumption zone and make the resolution requirements less demanding, but in the present study the original mechanism was used without modifications. The simulation was run for approximately two transient times. It required 340 000 processor hours of the ASCI QSC system at Los Alamos National Laboratory. The simulations used either 128 or 256 processors depending on the availability of the queuing system and took approximately four months to complete.

For future reference in the analysis of the flame edge results, it is necessary to obtain some additional one-dimensional flame values that are useful in the discussion of the results. Figure 2 shows the mass fractions of CH_4, O_2, H_2O, CO_2 and CO in a one-dimensional premixed planar flame (figure 2*a*) and a flamelet solution of (3.42) close to extinction (figure 2*b*). The premixed flame solution was obtained using the reduced mechanism with the compressible formulation and the values of the parameters previously discussed. The premixed planar flame was computed at the composition corresponding to the frozen flow mixture with mixture fraction equal to Z_s. For unity Lewis number, this is the appropriate mixture composition encountered ahead of the flame-edge head (Daou & Liñán 1998). We denote the premixed planar flame speed value as $S_{L,st}$ and numerical integration gives the non-dimensional value of 0.022. The resolution used in the calculation of the premixed planar flame was identical to that of the three-dimensional simulation and corresponds to 12 grid points for the hydrogen radical reaction rate. This resolution was found to be numerically appropriate. Finally, the diffusion flamelet structure in figure 2(*b*), was computed very close to the extinction limit, where the non-dimensional quenching scalar dissipation, χ_q, had a value approximately equal to 0.0205.

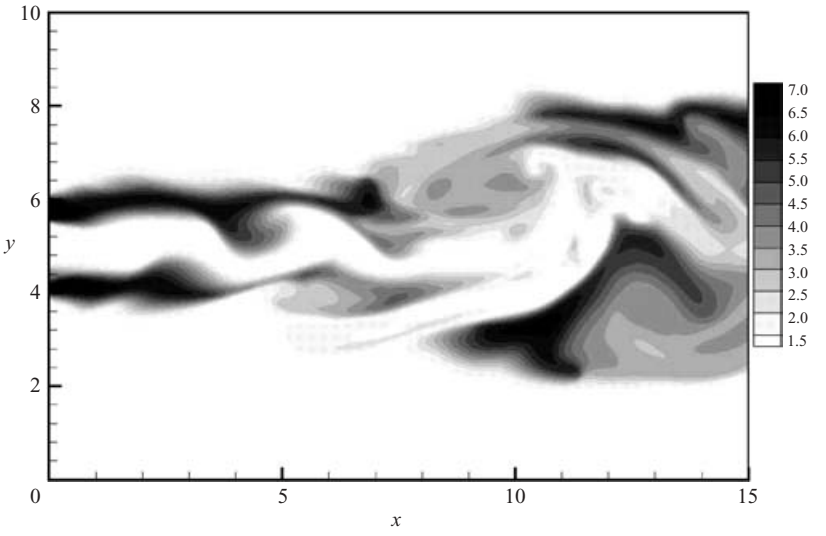

FIGURE 3. Temperature isocontours at plane through the centre of the domain at an instant in time.

4. Qualitative description of the flame

Turbulent flames, including the flame considered in this study, are complex three-dimensional objects that change in time owing to the unstable nature of the flow and to the effects of extinction and reignition. Figure 3 shows isocontours of temperature at the centre of the domain midway through the simulation. This figure is representative of the behaviour of the temperature field at other times. The parameters of this simulation were chosen to produce a flame that is partially extinguished and, in our case, this occurs predominantly around the centre of the domain. In this region, the large-scale organized vortices that are shed from the shear layers have sufficient strength, large rate of strain, to extinguish the flame. This is observed in figure 3, where low temperature values can be seen around the centre of the figure at both edges of the jet. The presence of these vortical structures that promote extinction in our flame are commonly seen in the near-field region of turbulent diffusion flames. Here, quasi-laminar flame structures envelop the jet core where vortical structures exist. This behaviour is observed in experimental and numerical observations of diffusion flames (Yule *et al.* 1980; Chen *et al.* 1991; Schefer *et al.* 1994; Everest, Feikema & Driscoll 1996; Takahashi *et al.* 1996; Yamashita, Shimada & Takeno 1996). Using a reactive Mie scattering technique, Roquemore *et al.* (1987) showed the existence of these vortical structures entrapped within the jet core edges and surrounded by the flame in the near-field region. In a comparative study by Clemens & Paul (1995) where both non-premixed reacting and non-reacting jets were analysed, it was also found that the near field consisted of laminar regions surrounding the inner core, where organized vortical structures were visible. Comparing experimental results for reacting and non-reacting jets, they show that the strong density gradients induced by combustion are responsible of extending the potential core. Large-scale organized vortical structures are also seen in the experimental measurements of $CH_4/H_2/N_2$ flames by Bergmann *et al.* (1998). Laser induced fluorescence intensity of NO shows the presence of these structures at the edges of the jet core, which is formed by the shear layers separating the fuel from the oxidizer. In our piloted flame, the region close to the inflow where the pilot is still

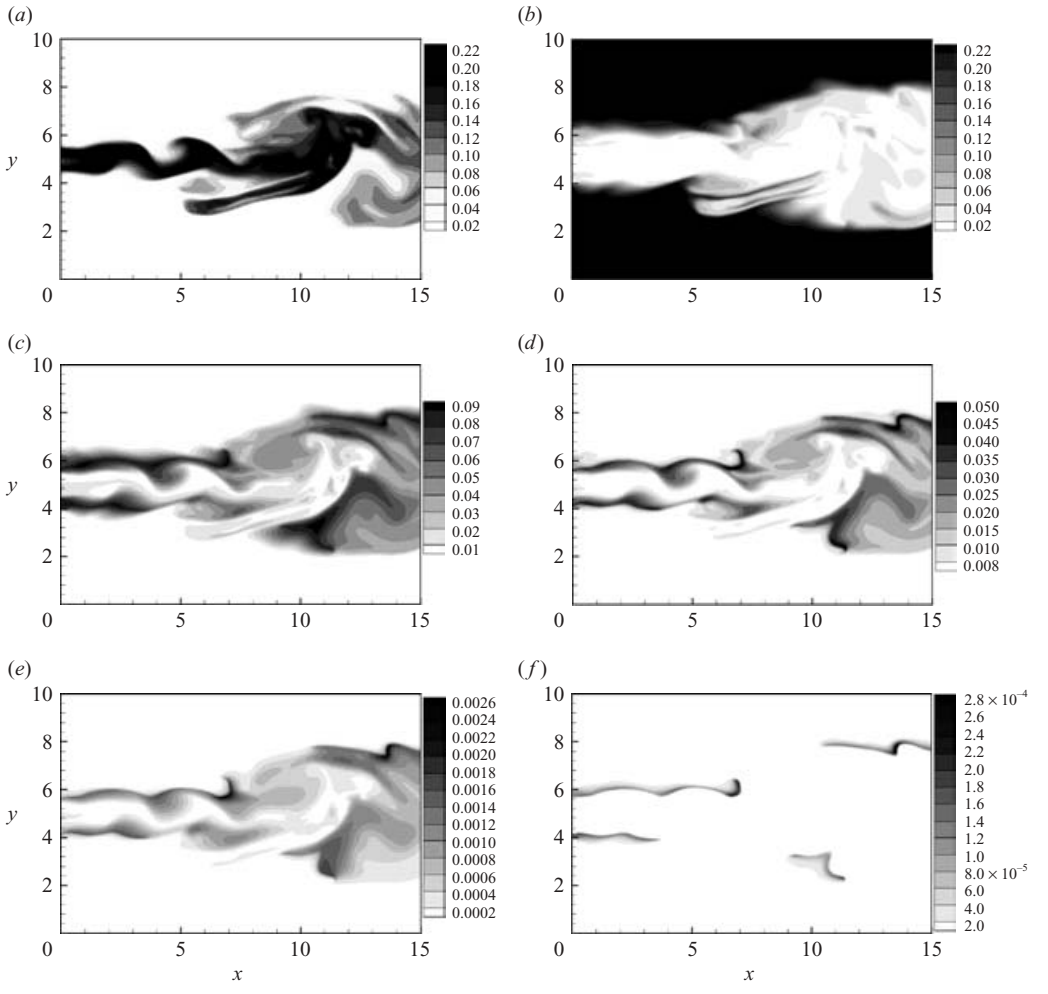

FIGURE 4. Species mass fraction isocontours at a plane through the centre of the domain at an instant in time. (*a*) Methane, (*b*) oxygen, (*c*) water, (*d*) carbon monoxide, (*e*) molecular hydrogen and (*f*) hydrogen radical.

strong is approximately laminar. However, the extent of this region is reduced here because the inflow forcing we use is strong. We chose this level of forcing to reduce the extent of the potential core so that the usefulness of the computational domain is maximized to capture more turbulent flow within the box. As an aside, it has been shown that the region close to the nozzle experiences stronger differential diffusion effects (non-unity Lewis number effects) owing to the quasi-laminar behaviour of the flame (Bergmann *et al.* 1998). In round jets, this region extends from the nozzle to $x/D \approx 10$, where D is the diameter of the jet and the effects of differential diffusion remain even at larger distances from the nozzle (Pitsch 2000). In our flame, it is anticipated that differential diffusion effects are important within the complete length of the domain.

4.1. *Distribution of flame composition and extinction*

Figure 4 shows mass fractions, at the same time and location, of methane, oxygen, water, carbon monoxide, molecular hydrogen and hydrogen radical. Plots of carbon

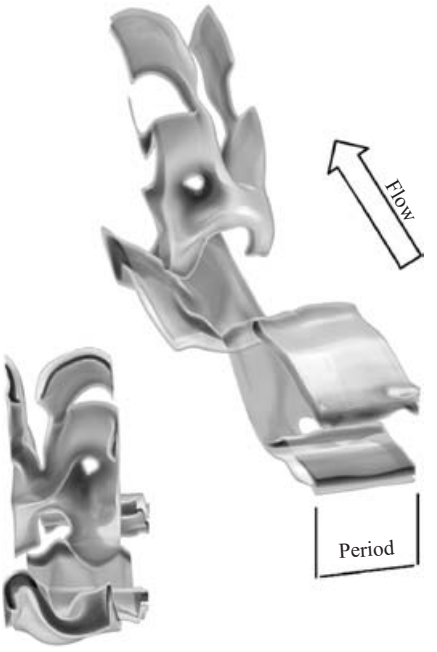

FIGURE 5. Three-dimensional rendering of hydrogen radical mass fraction at an instant in time.

dioxide are not shown because they are very similar to those of water in this flame. The extinguished regions are clearly seen in figure 4(f), where gaps in the hydrogen radical mass fraction reflect extinction. In our flame, hydrogen radical is the only radical of the flame.

Availability of the hydrogen radical field facilitates geometrical studies of the flame because, in our case, although a flame is more complicated than just a one-field quantity, it can be identified well with the flame. Figure 5 shows the hydrogen radical mass fraction field at one instant in time with the observer at two different angles. This figure is a three-dimensional volume rendering of the field, where the magnitude of the mass fraction determines the opacity of the zones. A nonlinear mapping was used to highlight the regions of very large radical concentration. The images were generated by volume rendering graphic cards from the Center for Advanced Computing Research (CACR) at Caltech. The view angle of figure 5(a) corresponds approximately to that of an observer placed in the general direction of the jet and is slightly above the exit plane. Figure 5(b) is a frontal view of the flame, the jet is coming towards the observer. In both figures, the hydrogen radical mass fraction shows the large extinguished region in the centre of the flame and the formation of multiple holes of varying geometries. The regions of high mass fraction, shown in dark contrast, were typically seen around vividly burning flame edges, as in closing holes, and were absent in regions that were undergoing extinction. The peak value of hydrogen radical mass fraction around closing holes or advancing edges was typically four to five times higher than the values observed in the other regions of the flame. Note that some large holes in the flame, primarily in the upper region, appear unclosed. This is because the flow is periodic in the spanwise direction and, at this time, the apparently missing section of the hole lies on the other side of the computational domain. Visualizations of the heat release rate from the DNS of Mahalingam *et al.* (1995) and Bédat *et al.* (1999) also indicate the

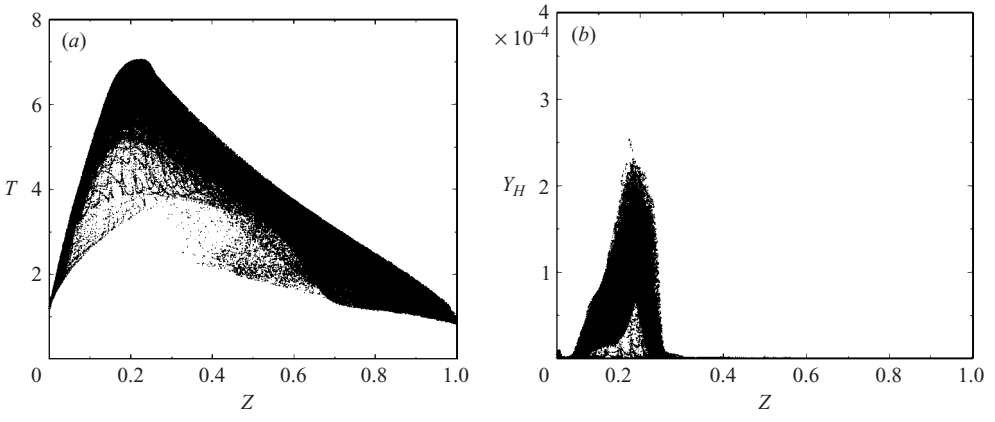

FIGURE 6. Scatter plot of (*a*) temperature and (*b*) hydrogen radical mass fraction versus mixture fraction at $x/H = 11$.

presence of holes in a diffusion flame submerged in a homogeneous turbulence field using a synthetic chemical mechanism. The differences between our study and that of Bédat *et al.* (1999) reside in the chemical mechanism and the flow configuration.

Figure 6 shows scatter plots, collected in time, of temperature and hydrogen radical mass fraction versus mixture fraction at the fixed streamwise location of $x/H = 11$. As can be seen in figure 6(*a*), temperature dependence on mixture fraction shows large scatter between the equilibrium values (upper envelope) and the frozen flow value (lower envelope). Figure 6(*b*) is complementary to the temperature and shows large scatter on hydrogen radical mass fraction owing to the constant extinction/reignition of the flame.

4.2. *Pilot stabilization mechanism*

The role of the pilot in the stabilization of the flame and the choice of parameters are discussed next. Pilots are typically used in diffusion flame jets at sufficiently large Reynolds numbers because the rate of scalar dissipation is maximum close to the burner exit plane and decreases with increasing distance downstream. In these flows, the flame is unable to maintain the high temperatures required for combustion close to the burner exit without an additional heat source. Furthermore, for cold reactants (our case) typical hydrocarbon flames are unable to autoignite downstream and we are left with a turbulent non-reacting jet. An approach used frequently in experimental investigations is to surround the main jet by a slower hot flow resulting from secondary combustion of another fuel. This low-momentum flow, low density and high temperature, is typically composed of a mixture of reaction products and oxygen (Barlow & Frank 1998) and it is called the pilot flame. When the main jet comes into contact with this hot flow, a flame is established and burns independently of the rate of scalar dissipation because the high temperature that control the typical Arrhenius nonlinear reaction rates is maintained externally. The temperature of the hot products decreases gradually with increasing distance until the flame starts to burn at a rate controlled by the scalar dissipation (that now is only a fraction of its value at the burner exit). This technique is well suited to flows at high Reynolds numbers where extinction can take place further downstream of the burner exit through the locally large rate of strain caused by the intermittent nature of turbulence. In the context of numerical simulation, the difficulty with this technique is that the effect

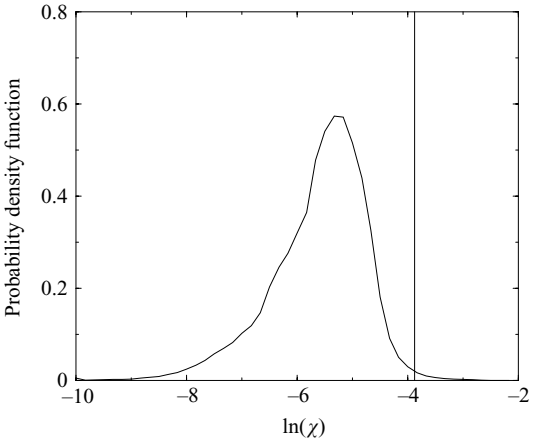

FIGURE 7. Conditional scalar dissipation p.d.f. at $Z = Z_s$ in the pilot controlled region, $x/H < 2$. The thick vertical line denotes the quenching limit from the flamelet equation.

of the pilot is felt for a relatively large distance from the burner exit and direct simulations require prohibitively large domains.

For lower-Reynolds-number flows, it is possible to create a pilot that consists of an ignition source located at the burner exit plane (Yamashita *et al.* 1996). This is modelled in our simulation through the boundary conditions detailed in § 3.3, by maintaining the temperature high and the scalar dissipation low around the pilot inflow region. With this technique, it is found that for given Reynolds and Damköhler numbers there is a parameter window, pilot thickness and velocity, over which the flame can be stabilized and, at the same time, the influence of the pilot can be limited to a short region downstream of the burner exit. In this transitioning regime of piloted flames, we can reliably stabilize the flame if the inflow parameters are well controlled; the case of a numerical simulation. In the present study, the parameters of the pilot were determined by performing a number of two-dimensional simulations until the jet evolution was satisfactory.

Quantitative evidence that the pilot used in this study releases only small amounts of energy is evident in figure 5. In that figure, it can be seen that a flame hole forms in the lower pilot flame of the jet, close to the inflow. Several holes are formed during the course of the simulation, but they are unable to tear apart the pilot flames. The presence of these flame holes is evidence that the amount of energy introduced by the pilot is limited. The pilot flame is only broken apart when it encounters the first strong vortical structures in the centre of the domain. The strength of the pilot at the inflow can be inferred from figure 7, where the scalar dissipation p.d.f. conditioned on the stoichiometric surface in the region $x/H < 2$ is shown. Here, the scalar dissipation is maintained mostly below the extinction limit, shown as a thick vertical line, owing to the quasi-laminar state of the flow. The higher temperature and associated higher viscosity and diffusivity generated by the pilot flame renders the local flow more stable and that helps to limit the magnitude of the scalar gradients. It appears that this is the mechanism by which the pilot flame is sustained.

The stabilization of the main flame further downstream, the region of interest in this study, is caused by the intermittently broken pilot flames. When the pilot flame is broken by the first large-scale vortex, occurring in the region $3 < x/H < 5$, flame segments are convected downstream until they aggregate to the main flame. This

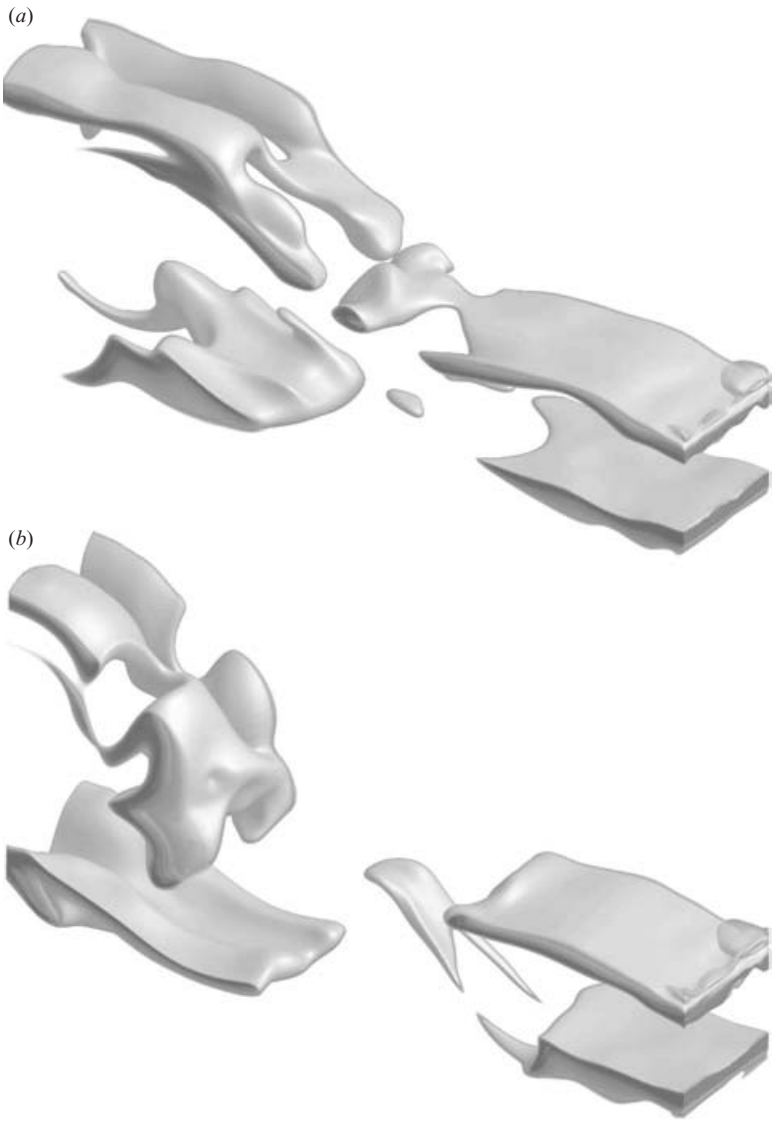

FIGURE 8. Three-dimensional renderings of hydrogen radical mass fraction showing the pilot flame annexation. (*a*) Top and (*b*) bottom pilot flame annexation events.

happens in the simulation at more or less regular intervals and helps to stabilize the main flame. Figure 8 shows a hydrogen radical mass fraction rendering at instants at which pilot flame segments are observed in the middle of the domain. These flame segments travel downstream and contribute to the global stability of the main flame by joining it and increasing its flame surface. This stabilization mechanism is due to direct flame annexation.

5. Statistical characterization of the flow

In this section, we provide some statistical characterization of the flow. We define the characteristic flow transient time as $t_L = L_x/U_j$. Experience with this and other

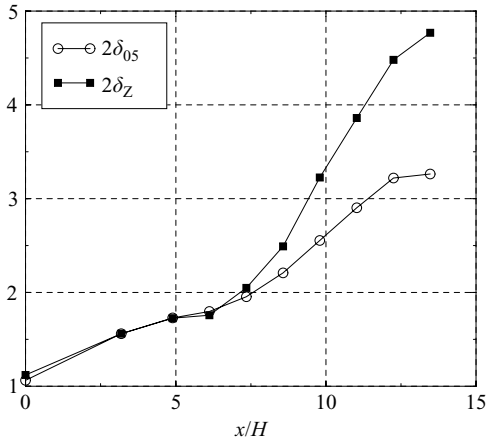

FIGURE 9. Average velocity and mixture fraction jet thickness dependence on streamwise coordinate.

kinds of turbulent flows show that, in order to achieve well-converged first-order statistics one must sample the flow for approximately $10\,t_L$ (Stanley *et al.* 2002; Jiménez 2003). In our case, such a simulation would have required approximately two years of computational time, with our present resources, and it is simply unattainable at this time. For this reason, we were able to run the simulation for approximately $2\,t_L$ and we do not assert that statistical averages of all quantities extracted from the database are well converged, but we believe that the present results are sufficient for the study of extinction dynamics. This is a phenomenon occurring at the smallest scales of the flow, and averaging on time and across space on these regions gives reasonable statistical information. The parameters of the simulation were selected in order to obtain sufficient extinction for averaging across these structures. Given these limitations and in order to characterize the flow to some extent, we provide in this section some Favre-averaged mean quantities.

Mean velocity, scalars, turbulence kinetic energy and scalar variances at different sections across the flow are presented next. The average value of an arbitrary function ψ is computed as a simultaneous temporal and spanwise direction means,

$$\bar{\psi}(x, y) = \frac{1}{N_T N_z} \sum_{j=1}^{N_T} \sum_{i=1}^{N_z} \psi(x, y, z_i, t_j), \tag{5.1}$$

where N_T is the number of time steps over which the average is computed. Favre averages, $\tilde{\psi} = \overline{\rho\psi}/\bar{\rho}$, and Favre fluctuations, $\psi'' = \psi - \tilde{\psi}$, are defined in the usual way. All average values reported in this section were computed from $t = 5$ to $t = 30$. The values at the beginning of the simulation are not used in the calculation of the averages because the flamelet solution is still adapting to the flow conditions. Statistics concerning extinction dynamics are postponed to the following section.

Figure 9 shows the average jet width as a function of the streamwise coordinate. Two measurements of the jet width are provided in this figure: δ_{05} is the width based in the 50% mean streamwise velocity profile and δ_Z is the width based on the 50% mean mixture fraction profile. Both thickness measurements are similar up to $x/H \sim 7$, but δ_Z becomes larger than δ_{05} beyond this point. These results are consistent with those of Stanley *et al.* (2002) for non-heated planar jets. They also observe a transition in

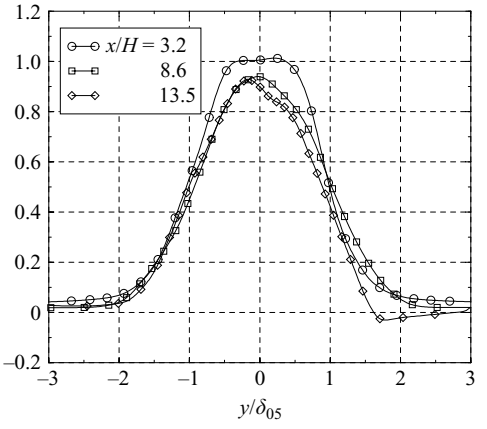

FIGURE 10. Average velocity at different streamwise positions.

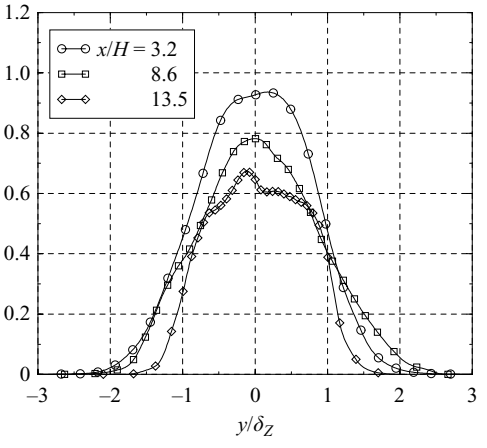

FIGURE 11. Average mixture fraction at different streamwise positions.

growth rate around $x/H \sim 7$ and a faster rate of mixing for the scalar profile beyond this point when compared to the rate of spread of the velocity profile.

Average streamwise velocity and mixture fraction profiles are shown in figures 10 and 11 at three stations, $x/H = 3.2, 8.6$ and 13.5. It is observed that the mixture fraction profiles diffuse faster than the velocity profiles, similar to the results found in DNS of nonheated planar jets. Figure 12 shows average temperature profiles at the same stations. It is seen that the average temperature is large, close to the adiabatic flame temperature, in the piloted region of the flame close to the inflow. In the intermediate station, the mean temperature is low owing to the large amount of extinction that takes place at and around $x/H = 8.6$. At the later station, $x/H = 13.5$, the temperature is higher than that of the preceding station owing to the lower level of extinction in this region.

Figure 13 and 14 show average turbulence kinetic energy, $\tilde{k}$, and mixture fraction variance, $\widetilde{Z''^2}$, respectively. It is observed that the level of turbulence fluctuations increases with increasing distance from the inflow plane. The mixture fraction fluctuations also increase with increasing distance from the inflow plane, but it starts to decrease at the last station. This is consistent with the larger rate of mixing observed

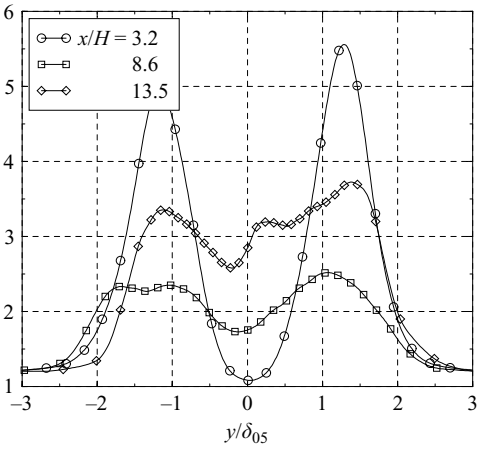

FIGURE 12. Average temperature at different streamwise positions.

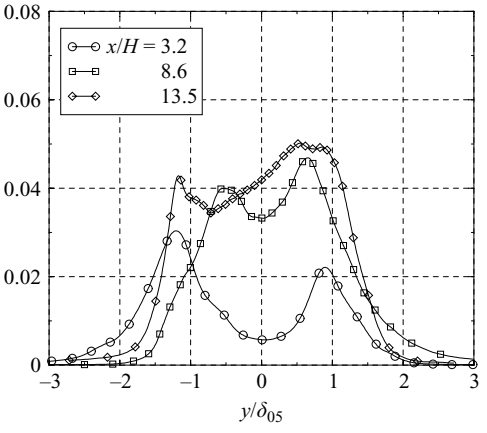

FIGURE 13. Average turbulence kinetic energy at different streamwise positions.

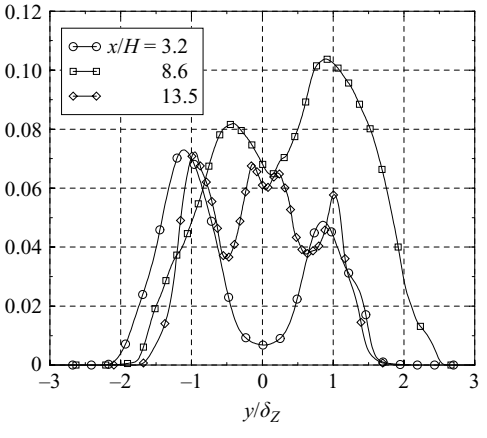

FIGURE 14. Average mixture fraction variance at different streamwise positions.

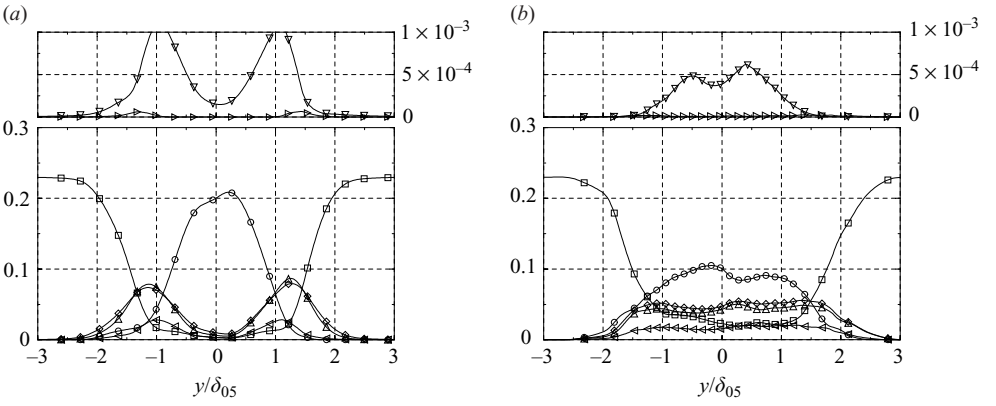

FIGURE 15. Average composition mass fractions at (*a*) $x/H = 3.2$ and (*b*) $x/H = 13.5$. ○, CH_4; □, O_2; ◇, H_2O; △, CO_2; ◁, CO; ▽, H_2 and ▷, H.

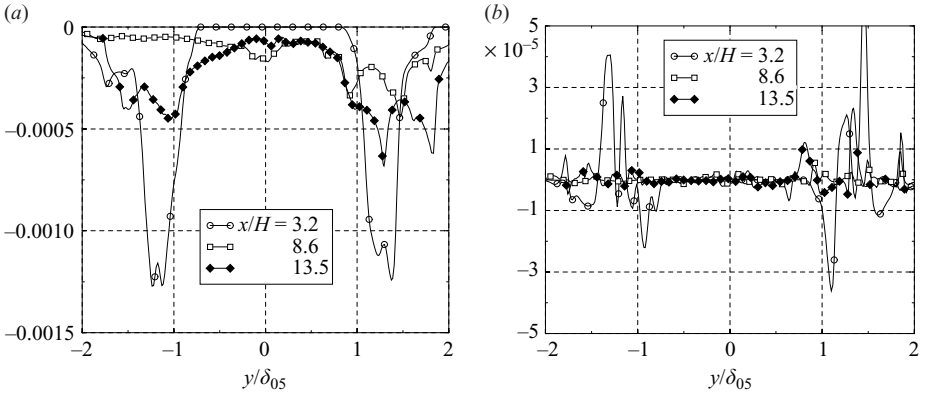

FIGURE 16. Average reaction rates of (*a*) CH_4 and (*b*) H at different values of x/H.

in figure 9. The results of figure 13 and the turbulence dissipation, $\tilde{\epsilon}$, that are not shown here, give an estimate of the turbulence Reynolds number, $Re_t = u_{rms}l/\nu$ where $l = u_{rms}^3/\tilde{\epsilon}$ and $u_{rms}^2 = 2\tilde{k}/3$. These quantities varied across the jet width and reached a peak, in most cases, around the centre of the jet. Our statistics give a peak Re_t around 300 at $x/H = 3.2$ and $x/H = 13.5$ and a value around 500 for $x/H = 8.6$. The reason the Reynolds number is large around the centre of the computational domain is probably caused by two effects. First, in this region the flame is predominantly extinguished with low temperature and high density. Secondly, the strong dependence of the viscosity with temperature creates a low-viscosity region at the centre of our domain. These effects contribute to a larger value of the turbulence Reynolds number.

Figure 15 shows average composition mass fractions (*a*) close to the inflow plane and (*b*) close to the outflow plane. Figure 15(*a*) shows that the flame is almost planar in the piloted region close to the inflow, with negligible amounts of products at the core of the jet. On the other hand, figure 15(*b*) shows that substantial mixing has taken place at this station. Furthermore, figure 16 shows the average reaction rates of methane and hydrogen radical at different distances from the inflow plane. It is seen that the methane reaction rate is relatively compact close to the inflow plane,

it becomes very small in the central region where large-scale extinction is present and becomes broader further downstream where the flame is burning again and it is being stirred by turbulence. On the other hand, the reaction rate of hydrogen radical behaves differently. In fact, while the reaction rate average is relatively compact close to the inflow plane, it becomes almost negligible far downstream. This behaviour, at first puzzling, is a consequence of the dependence of the hydrogen radical reaction rate on the spatial coordinates. The reaction rate of hydrogen radical has both positive and negative parts. When averaging in time is applied at a specified location in space, these positive and negative contributions tend to cancel each other out. This results in very small values of the average reaction rate for the radical. This is not observed for major species because the reaction rates are predominantly positive for products and negative for reactants. Although our results are not conclusive owing to our limited sampling, it is clear that if these observations results are correct, the implications for modelling purposes are important.

There have been some attempts to model chemically reacting flows by solving averaged transport equations for all the chemical species. In this approach, the average reaction-rate terms must be modelled somehow. This methodology is commonly referred to as the direct-closure approach and constitutes the turbulent-combustion-closure problem, properly speaking. Our statistics indicate that attempts to model average radical reaction rates are futile, because the positive (production) and negative (consumption) parts of typical radical reaction rate functions combined with the spatial and temporal variability of turbulent flows produce average rates that are not representative of their instantaneous values. This is important because it implies that one cannot model average radical reaction rates from the knowledge of the rates provided by the detailed chemical mechanism.

6. Flame-edge statistics

A turbulent flame is a complex geometrical object. We can think of it as a coupled multiscalar manifold with changing topology. The coupling originates in the reaction rate terms that represent chemical conversion and affect in a direct way the temperature, density and mean molecular weight. These direct variations, primarily in density, but also in molecular properties through variations of the temperature, induce indirect changes in the velocity field. These velocity variations can, in turn, affect the rates at which reactants and products are brought together and removed from the flame, respectively. This coupling is generally referred to in the literature as the turbulence–chemistry interaction. Depending on the combustion regime, several theoretical abstractions have been used to understand this coupling. For example, it has been proposed (Williams 1975) that, under the appropriate conditions of large Damköhler numbers, the flame becomes very thin. In this case, the geometry of the flame is relatively well defined by a surface, the so-called flame sheet.

The results of the present study support, to some extent, the idea that even for diffusion flames under relatively large rates of strain, the flame remains quite thin (see figure 4*f*). We are certainly assuming that the mass fraction of hydrogen radical can be realistically used as a marker of the flame. In our case, there are only a few meaningful fields that could be used to identify the flame. It is common to use the heat release rate to associate the regions where the flame burns vigorously with the flame location, see Im & Chen (2001) for an example. In our case, a quick review of the algebraic form of the reaction rates of the reduced mechanism used in this study reveals that all these rates are proportional to the concentration of hydrogen

radical. Some differences between the hydrogen radical field and the heat release rate are bound to exist, specially during short transients. These transients are likely to appear at the instant a hole is formed and also when a hole collapses. In the first case, as soon as these extinguished regions grow, the hydrogen radical will diffuse and accommodate around the flame edges and disappear from the completely extinguished region. In the second case, it has been shown that the collapse of flame holes is a very fast process (Buckmaster & Jackson 2000; Pantano & Pullin 2003) and it should not have a statistical impact on the results. Thus, we expect that, apart from these very short transients, the hydrogen radical mass fraction is a reasonable indicator of our flame location. We would like to stress that this choice is by no means unique and involves some degree of uncertainty.

Two statistical quantities are investigated in this section. First, we determine the total flame area evolution with time within the computational domain. Secondly, once the flame edges are identified, the joint flame-edge velocity-scalar dissipation probability distribution (p.d.f.) is recovered.

6.1. *Flame identification*

We assume that the external structure of the flame is approximately defined by the mixture fraction field, such that the flame lies around a mixture fraction surface, $Z(x_1, x_2, x_3, t) = Z_o$, where Z_o is close to Z_s. This definition is appropriate far from extinction and when the Lewis number of all species is one (Williams 1985). In our case, detailed visualization of the flame structure shows that this definition is still appropriate, even though the Lewis number is not unity (see beginning of § 4), provided the extinguished surface regions are removed. This is simply accomplished by recognizing that the mass fraction of hydrogen radical is negligible in those regions. We define three subspaces, according to

$$\mathscr{S}(t) = \{(x_1, x_2, x_3) \in \mathbf{R}^3 : Z(x_1, x_2, x_3, t) = Z_o\}, \tag{6.1}$$

$$\mathscr{F}(t) = \{(x_1, x_2, x_3) \in \mathbf{R}^3 : Z(x_1, x_2, x_3, t) = Z_o, \quad Y_{\mathrm{H}}(x_1, x_2, x_3, t) > Y_s\}, \tag{6.2}$$

$$\mathscr{E}(t) = \{(x_1, x_2, x_3) \in \mathbf{R}^3 : Z(x_1, x_2, x_3, t) = Z_o, \quad Y_{\mathrm{H}}(x_1, x_2, x_3, t) = Y_o\}, \tag{6.3}$$

where $\mathscr{S}(t)$ is the two-dimensional manifold defining the stoichiometric surface, $\mathscr{F}(t)$ is the two-dimensional manifold defining the flame and $\mathscr{E}(t)$ is the one-dimensional manifold defining the flame edges. $\mathscr{F}(t)$ is a three-dimensional surface with holes and $\mathscr{E}(t)$ is composed of multiple open and closed loops. The parameter Y_o is a threshold of the hydrogen radical mass fraction and it has been chosen after extensive visualization of the flame edges and is typically 5 to 10% of the peak hydrogen radical mass fraction on the flame, in our case $Y_o = 3 \times 10^{-5}$. This value has proved to give very reliable results regarding identification of the flame and flame edges, except at those location and instants when a hole is created. These occurrences cannot be detected accurately with the present algorithm, but they do not represent a large fraction of the edges in terms of sampling numbers and they are removed from the statistics. It was found that using the hydrogen radical field produced more reliable identification of the flame edges than when the heat release rate was used. This seems to be due to the complex structure of the heat release rate around edges (Ruetsch *et al.* 1995). Finally, a comparison of the flame surface determination based on the Bilger, Stårner & Kee (1990) mixture fraction variable was carried out and no meaningful differences were observed. Both mixture fractions give equally good flame surface approximations. This is probably due to the manner in which the flow is initialized, since both the initial flow and the forcing are mapped to Z. Using the previous definitions, we

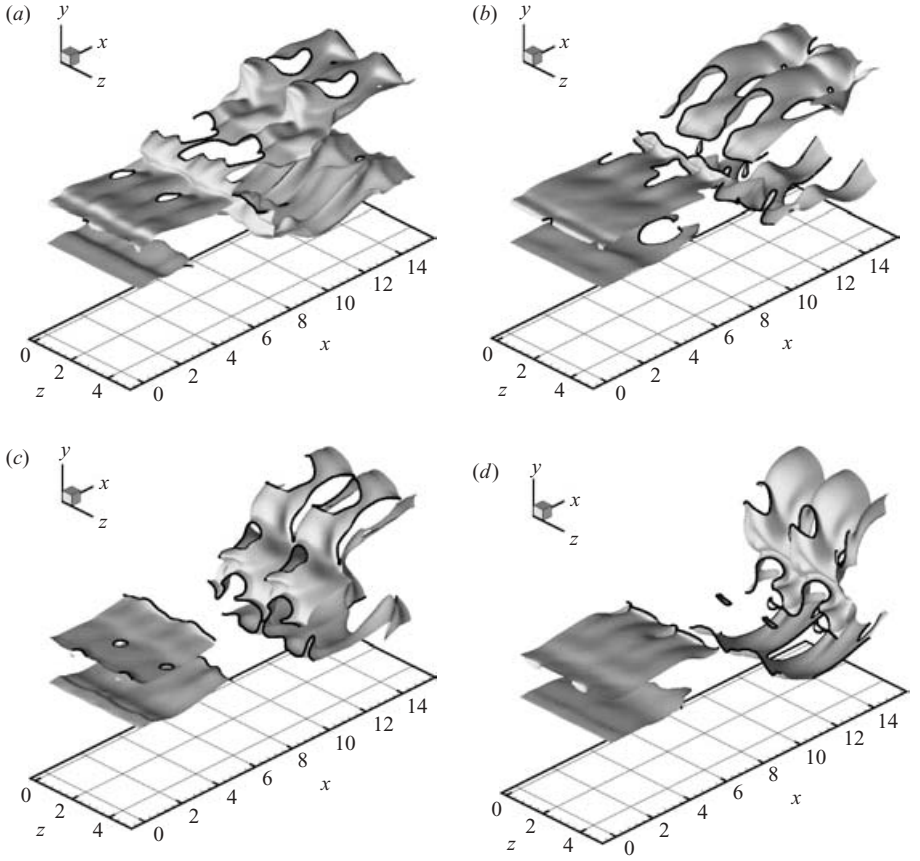

FIGURE 17. Flame surface and edge geometry at four times during the simulation.

developed an algorithm that extracts $\mathscr{F}(t)$ and $\mathscr{E}(t)$. The algorithm is described in detail in Pantano & Lombeyda (2003). Further details regarding the effect of varying isosurfaces are reported in the Appendix. The following flame surface visualization and statistics correspond to case (ii) in the Appendix.

Figure 17 shows the flame surface $\mathscr{F}(t)$ and the flame edges $\mathscr{E}(t)$, thick black lines, at several instants in time during the simulation. The jet runs from left to right and the two flames at the opposite sides of the jet are visible. Since the domain is periodic in the spanwise direction, two copies of the flame are shown as a visual aide to help in the interpretation of the surface geometry. The region to the left shows the well-defined pilot stabilized region. Figure 17(a) corresponds to time $t = 0.3t_L$, after the initial adjustment of the flamelet profiles. Figures 17(b)–17(d) correspond to $t = 0.8t_L$, $1.3t_L$ and $1.8t_L$, respectively.

In order to make more quantitative measurements, we define the area operator by

$$A(\mathscr{X}) = \int_{\mathscr{X}} \mathrm{d}\mathscr{X}, \tag{6.4}$$

where $\mathscr{X}$ is the surface manifold coordinates in the three-dimensional space and $\mathrm{d}\mathscr{X}$ denotes the area differential. The postprocessing algorithm was used to extract a burning index defined as the ratio of flame area to stoichiometric surface area,

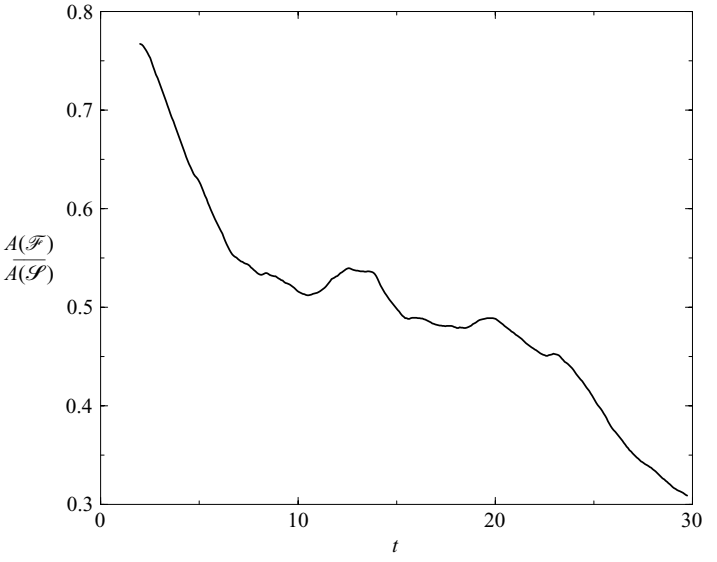

FIGURE 18. Burning index evolution with time.

given by

$$r = \frac{A(\mathscr{F})}{A(\mathscr{S})}. \tag{6.5}$$

Figure 18 shows the burning index, r, as a function of time. The values of r during the first instants of the simulation are not reported because the algorithm was unable to reliably predict the burning flame surface. This is due to the strong transient effects introduced by the relaxation of the initial flamelet profiles to the correct values. Figure 18 shows that, initially, r has a relatively high value, owing to the artificial initial condition, and decreases strongly. Then, r stabilizes somewhat, from $t = 5$ to 20. This relatively calm period is followed by a further decrease of r. The origin of this decrease is partially due to the presence of a large-scale organized vortex that wraps the flame and convects a large portion of the burning flame outside the domain, and makes the value of r temporarily low. Availability of more powerful computational resources in the future will certainly allow larger computational domains and times to extend the current results further. Nevertheless, the central period of our simulation, where r is relatively uniform, can confidently be used to extract meaningful statistical data about the flame edges since the total flame area does not change much.

6.2. *Flame-edge velocity statistics*

At this point, we will use the previously detected flame edges to extract statistics about the flame-edge velocity. We start by defining the unitary normal directions to the mixture fraction and hydrogen radical mass fractions isosurfaces

$$\boldsymbol{n}_Z = \frac{\nabla Z}{|\nabla Z|}, \tag{6.6}$$

$$\boldsymbol{n}_{\mathrm{H}} = \frac{\nabla Y_{\mathrm{H}}}{|\nabla Y_{\mathrm{H}}|}, \tag{6.7}$$

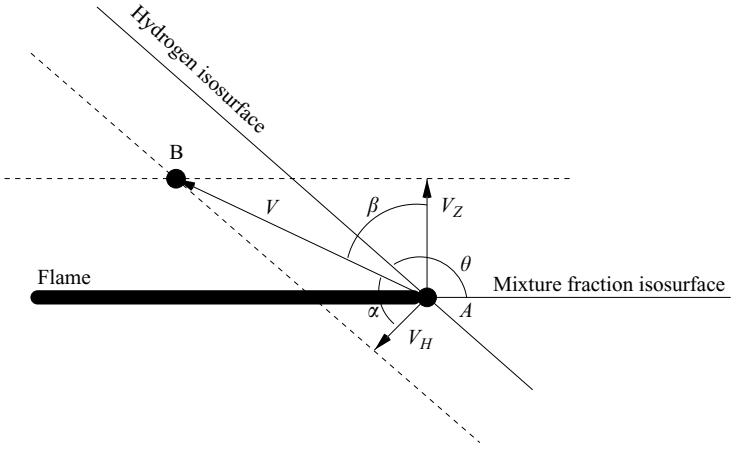

FIGURE 19. Geometrical determination of the edge velocity.

respectively. The normal velocity of the isosurfaces can be determined from knowledge of the transport equations of the respective fields and they are given by

$$V_Z = \boldsymbol{u}\cdot\boldsymbol{n}_Z - \frac{\nabla\cdot(\rho D_Z \nabla Z)}{\rho|\nabla Z|}, \tag{6.8}$$

$$V_{\mathrm{H}} = \boldsymbol{u}\cdot\boldsymbol{n}_{\mathrm{H}} - \frac{\nabla\cdot(\rho D_{\mathrm{H}} \nabla Y_{\mathrm{H}}) + \dot{\omega}_{\mathrm{H}}}{\rho|\nabla Y_{\mathrm{H}}|}, \tag{6.9}$$

for mixture fraction and hydrogen radical mass fraction, respectively. The diffusivities of mixture fraction and hydrogen radical are given by $D_Z = \delta^*(T)/(Re\,Sc)$ and $D_H = \delta^*(T)/(Re\,Sc_H)$, respectively. Notice that both the flow velocity and the normal direction intervene in the definitions. Moreover, it is well known that only the normal velocity of the isosurfaces can be uniquely defined. It is not uncommon to complement the normal velocity with the component of the flow velocity tangential to the normal. In doing so, a full three-dimensional velocity vector can be associated at each isosurface point (Gibson 1968). Here, we do not require this extension of the isosurface velocity because the normal velocity suffices. Figure 19 shows a generic geometric disposition of the isosurfaces, the normal velocities and the edge displacement. Note that this figure only shows one of the possible cases, that in which the sign of V_{H} is positive, that is, the isosurface velocity is in the same direction as the normal. The case in which V_{H} is opposite to $\boldsymbol{n}_{\mathrm{H}}$ ($V_{\mathrm{H}} < 0$) is also possible and leads to a similar geometrical treatment with some angles that are complements of those shown in figure 19. For compactness, we show the derivation for the case where $V_{\mathrm{H}} > 0$ shown in figure 19. The angles α and β denote the angles of the normals to the edge velocity vector, determined in the figure by the vector that goes from point A to B. These angles are related to the angle between the normals, θ, by

$$\theta = \alpha + \beta, \tag{6.10}$$

where

$$\cos\theta = \boldsymbol{n}_Z \cdot \boldsymbol{n}_{\mathrm{H}}. \tag{6.11}$$

These angles can be used to relate the velocity of point A, V, to those of the isosurfaces, through

$$V\cos\alpha = V_{\mathrm{H}}, \tag{6.12}$$

$$V\cos\beta = V_Z. \tag{6.13}$$

Equations (6.10)–(6.13) can be manipulated to obtain explicit relations for V, α and β in terms of θ, V_H and V_Z. At this point, we define the relative velocity of the flame edge, V_o, as the projection of V on the stoichiometric surface with the convention that positive V_o implies edges travelling in the direction of the extinguished region and it is defined by

$$V_o = -V\cos\left(\tfrac{1}{2}\pi - \beta\right). \tag{6.14}$$

In order to determine what is called the flame-edge speed, similar to the definition used by Ruetsch *et al.* (1995), in our approach we must take into account the velocity of the flow incoming towards the edge. This velocity is given with our convention by

$$u_m = \boldsymbol{u}\cdot\boldsymbol{m}, \tag{6.15}$$

where $\boldsymbol{m}$ is the unitary tangent vector at the edge,

$$\boldsymbol{m} = \boldsymbol{n}_Z \times (\boldsymbol{n}_H \times \boldsymbol{n}_Z).$$

Note that u_m is positive in the opposite direction to V_o, that is, in the direction of the burning region. With all these definitions at hand, the flame-edge velocity is given by

$$V_e = V_o + u_m. \tag{6.16}$$

Other works (Ruetsch *et al.* 1995; Im & Chen 1999) have used a procedure that is very similar to that introduced above, equations (6.6)–(6.16), to determine the velocity of intersecting isolines. In our case, apart from the fact that the edges are three-dimensional, our choice of scalar fields is different and we project the velocity back to the stoichiometric surface to satisfy the premise that the edges are supposed to move on this surface.

Equations (6.6)–(6.16) and the scalar dissipation χ were computed at each of the flame-edge locations extracted by the edge identification algorithm described previously. The data were accumulated from approximately 400 times to construct a joint p.d.f. Moreover, only the downstream half of the computational domain was used to compute joint statistics. This was done to avoid mixing the statistics from the pilot region, where edge dynamics may be different, with those of the region of interest downstream. Figure 20 shows a contourmap of the joint flame-edge velocity-scalar dissipation probability density function. The horizontal axis shows the flame-edge velocity in linear coordinates and the vertical axis shows the natural logarithm of the scalar dissipation at the edge. The equally spaced joint p.d.f. values are represented by different tonalities of grey. Although some statistical scatter is present, the joint p.d.f. is reasonably converged. It can be seen that the joint p.d.f. has a characteristic shape that resembles the form of the dependence of the edge velocity on scalar dissipation of laminar studies (Daou & Liñán 1998), but in the present study, unstationary effects are clearly visible. Note that the joint p.d.f. is effectively broad and we expect that this is a manifestation of the randomness of the flow. Moreover, it is seen that as the scalar dissipation becomes large, the only probable values of the joint p.d.f. are those for which the edge velocity, V_e, is negative, that is, receding edges or expanding holes. The quenching value of the scalar dissipation determined previously from the flamelet equation is shown here as a horizontal thick line for reference purposes. It

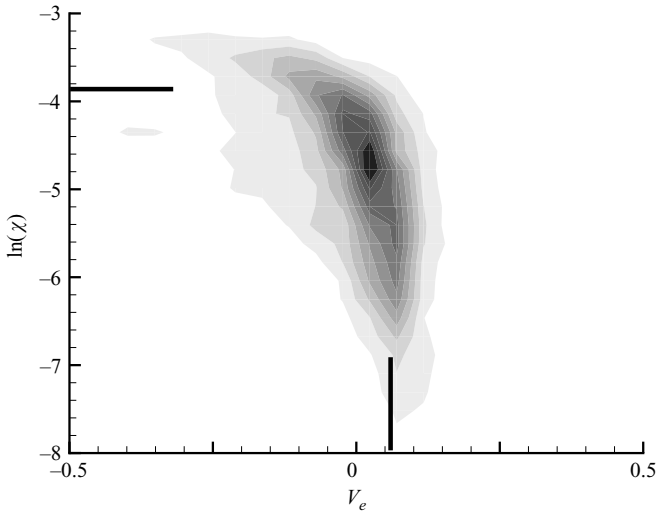

FIGURE 20. Joint flame-edge velocity-scalar dissipation p.d.f. The thick horizontal line represents quenching value of scalar dissipation, χ_q, and the vertical line represents stabilization flame-edge speed.

is expected that the flame ceases to exist for values of the scalar dissipation around the quenching value. In this figure, some edges propagating with negative velocities are encountered in the regions where χ is somewhat larger than the laminar quenching value, χ_q. This has been observed in the past by Mahalingam *et al.* (1995) in DNS of turbulent non-premixed combustion. They also identify the fact that the flow boundary conditions used in laminar calculations can influence the precise numerical value of the extinction limit. These boundary conditions cannot capture all unstationary and three-dimensional effects. For these reasons, we do not expect that the quenching value, χ_q, obtained from any specific one-dimensional configuration of the flame will give quantitatively accurate values in three-dimensional flows, though, typically the agreement is very good.

On the other limit of χ, as the scalar dissipation becomes small, the joint p.d.f. is non-negligible towards positive V_e. Based on previous works of two-dimensional simulation of edge flames, it is expected that this vertical asymptote should be centred around the stabilization edge speed. This speed is estimated here, following Ruetsch *et al.* (1995), as the product of the laminar premixed speed at the stoichiometric conditions, $S_{L,st}$, multiplied by the square root of the density ratio of the frozen flow, ρ_f, to that of the diffusion flame, ρ_b. The value we estimate is $S_{L,st}\sqrt{(\rho_f/\rho_b)} = 0.058$ and is shown in figure 20 as a vertical thick line. It can be seen that the peak of the joint p.d.f. is centred around this value in this region.

6.3. *Heat release rate statistics*

Among the multiple statistics that can be investigated in turbulent non-premixed combustion with extinction, the correlation between heat release rate and scalar dissipation has been the subject of increased attention. This correlation has been investigated in the past using DNS by Mahalingam *et al.* (1995) for one- and two-step chemistry and by Swaminathan *et al.* (1996) using single-step chemistry. They observe, in accordance with laminar theory (Peters 1984), that the heat release rate increases with increasing scalar dissipation. Figure 21 shows the conditional joint

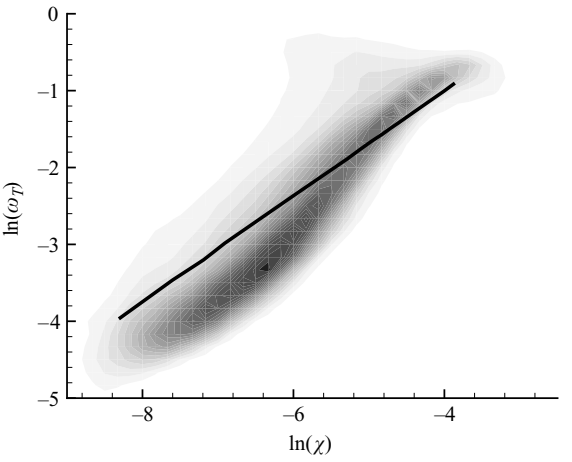

FIGURE 21. Conditional joint p.d.f. of heat release reaction rate and scalar dissipation at the stoichiometric mixture fraction, Z_s.

p.d.f. of heat release rate, $\dot{\omega}_T = -Da \sum_{i=1}^{N} h_i \dot{\omega}_i$, and scalar dissipation collected in a narrow band of thickness 0.02 in mixture fraction space around the stoichiometric surface, Z_s. This joint p.d.f. was compiled at the same times as the edge velocity–scalar dissipation joint p.d.f. and does not include the pilot flame, $x/H > 6$. The horizontal axis denotes the natural logarithm of the scalar dissipation and the vertical axis is the natural logarithm of the heat release rate. The isocontour levels are denoted in tonalities of grey; where the graduation from dark to light grey represent higher to lower uniform isolevels, respectively. The thick line on the same figure denotes the peak heat release rate as a function of scalar dissipation obtained from the flamelet equation, (3.42). The power law for this flamelet solution is approximately 0.685. In contrast, the conditional joint p.d.f. evolves approximately aligned with the direction of unity slope. These differences, apart from the broad character of the distribution caused by unstationary effects, probably originates from the contributions of the different modes of combustion in the flow; ranging from the burning flame edges to the extinction events. Since, in our regime of extinction, the number of flame edges/extinction events is important, their contribution to the statistics of the heat release rate are obviously present. It can be seen that at higher values of the scalar dissipation, the alignment with the flamelet solution is good. On the other hand, at lower values of the scalar dissipation, this alignment is less pronounced and the flamelet solution appears shifted upwards with respect to the joint p.d.f. In this region, we expect to encounter the contributions from the flame holes that are closing with positive flame-edge velocities; compare with figure 20. Here, the prevalent burning mode of the edge flames will contribute to the observed deviation of the p.d.f. statistics from the flamelet solution. The improved agreement of the flamelet solution for high scalar dissipation rates has been observed by Mell *et al.* (1994) in DNS of constant density reacting flows. They report that this is associated with an increase in the one-dimensionality of the reaction zone.

7. Discussion

Previous two-dimensional numerical works have investigated the mechanisms and parameters that determine the flame-edge velocity. In the case of stationary edges, this

velocity is well defined and Daou & Liñán (1998) give a detailed account for a one-step chemistry model with constant density. Other numerical works of unstationary flame edges subjected to the strain field of a vortex include Favier & Vervisch (1998), Im & Chen (1999) and Im & Chen (2001). In this case, a flame edge is approximately aligned with the centre of a vortex system and the edge propagates upstream or downstream depending on the relative strength of the vortex with respect to the chemistry. Boulanger & Vervisch (2002) studied the expected value of the Damköhler number at the tip of an edge flame, taking into account the ratio of the diffusive fluxes normal to the non-premixed flame to the premixed fluxes at the tip of the flame. They find that this ratio plays a role in the prediction of the flame-edge speed. In general, all studies agree that some measure of the mixture fraction gradient at the flame edge controls the propagation of the structure and that chemistry details cannot be neglected. In the present simulation, the analysis of the statistics suggest that, in three-dimensional flame edges, the scalar dissipation can be used to parameterize the edge speed. Unstationary effects are important and are reflected by a somewhat broad distribution function. These results can be exploited in advanced modelling of flame extinction/reignition through flame-edge propagation for turbulent combustion in two ways. First, we can neglect unstationary effects and assume that the edge-flame speed is determined uniquely by the local instantaneous value of the scalar dissipation. This function can be obtained from a two-dimensional boundary-value problem involving the chemistry, transport and heat release details for a certain canonical flow configuration, as in the works reported by Ruetsch *et al.* (1995) and Daou & Liñán (1998), as a function of the scalar rate of dissipation. This information can then be used to construct a triple-flamelet closure, first suggested by Dold, Hartley & Green (1991), by taking into account the statistics of the scalar dissipation at the stoichiometric surface. An example of this approach has been attempted by Pantano & Pullin (2004) for small flame holes. In the second approach, it may be possible to account for the unstationary effects on the flame-edge speed by either solving the corresponding joint-p.d.f. transport equation for flame-edge speed-scalar dissipation or adapting some of the ideas of the second-order conditional moment closure (CMC) method of Klimenko & Bilger (1999). In this latter case, additional correlations of the flame-edge speed due to unstationary effects caused by the statistics of the scalar dissipation could be retained.

Finally, of the two mechanisms that are thought to be primarily involved in reignition dynamics, flame-edge propagation and ignition through heat conduction from nearby hot products, only the former is discussed here. It can be seen in figure 20 that the simulation parameters were chosen appropriately to cover both expanding and collapsing holes. This is shown by the occurrence of both positive and negative values of the flame-edge velocity in the joint p.d.f. In the second mechanism, pockets of burned hot gases are convected and come into close proximity of fuel–oxidizer mixtures from the extinguished region leading to reignition. This mechanism cannot be captured in the present simulation. The reduced chemical mechanism used in this study is derived assuming that certain radical species are in quasi-steady state and that some reactions are in partial equilibrium. The species and reactions that are selected are appropriate for the burning regime but they are inappropriate for the quenched state (Peters 1985). In fact, Peters (1985) recommends that an alternative reduced mechanism should be derived if one is interested in the ignition phenomena. We can go back to the algebraic relations describing the reaction rates in § 3.2 and observe that the chemistry is controlled by the hydrogen radical. This radical can only exist around the flame and it is not encountered, in our flame, at any concentration in the extinguished regions. Thus, lack of hydrogen radicals make it impossible for this

flame to reignite, no matter how much time is given to the system. This limitation in our chemistry mechanism is recognized in the present study.

8. Conclusion

We report results of a direct numerical simulation of a turbulent non-premixed methane–air planar jet using a four-step reduced mechanism. Owing to the large cost of the simulation, the computational domain is restricted to the near-field region of the flow. The parameters of the simulation were selected to exhibit a non-negligible degree of extinction in order to study the dynamics of diffusion flame edges. The four-step reduced mechanism is the simplest reduced mechanism in the hierarchy of reduced mechanisms that includes radicals. In our case, the only radical that is computed along with the flow and stable species is the hydrogen radical.

Turbulence statistics were collected in time from the simulation database. It was found that average radical reaction rates in the more turbulent regions of the flow are negligible in comparison with their instantaneous contributions. This is because the radical reaction rates alternate signs across the flame and the fluctuating nature of the turbulent flow averages out most of the contributions to the average.

A feature identification algorithm was developed to extract flame-edge statistics from the simulation database. The flame is assumed to be spatially defined by the hydrogen radical mass fraction field. The flame edges are identified as the curves in space where a low-value isosurface of hydrogen radical mass fraction and the stoichiometric mixture fraction isosurface intersect. This geometric reduction approach was shown to give very reliable locations of the flame edges and holes. Knowledge of the transport equations of the scalar fields was then used to extract joint statistics of the flame-edge velocity and scalar dissipation (a local Damköhler number). It was found that while the peak of the joint p.d.f. of these two quantities bears some resemblance to the theoretically laminar flame-edge velocity relationship on scalar dissipation, substantial widening of the joint p.d.f. exists. This is presumably due to unstationary effects.

This work was supported in part by the ASC program of the Department of Energy under subcontract no. B341492 of DOE contract W-7405-ENG-48. The author would like to thank S. Lombeyda of the Center for Advanced Computing Research at Caltech for generating the three-dimensional hydrogen radical mass fraction figures. The author would also like to thank Professor D. I. Pullin for innumerable discussions and for reading and suggesting improvements to the manuscript. Additionally, the author would like to thank the referees for many comments.

Appendix. Edge-detection sensitivity

This Appendix addresses some of the heuristic details associated with the edge-flame-detection algorithm. The current scheme is based on an extension of the procedure outlined by Ruetsch *et al.* (1995) for two-dimensional flame edges. Instead of intersection of isolines, we must consider the intersection of isosurfaces in three-dimensional flows. In our flame, these isosurfaces are obtained from the mixture fraction and hydrogen radical mass fraction fields through (6.3). In order to quantify the impact of the isosurface values on the quality and uncertainty of the measured edge velocity we have conducted a limited parametric study by considering four sets of isosurface values. There is a limited range of mixture fraction values and hydrogen

Case	Z_o	Y_o
(i)	0.2	6×10^{-5}
(ii)	0.2	3×10^{-5}
(iii)	0.1875	3×10^{-5}
(iv)	0.16	3×10^{-5}

TABLE 3. Threshold values of Z_o and Y_o for parametric study of the edge-detection algorithm.

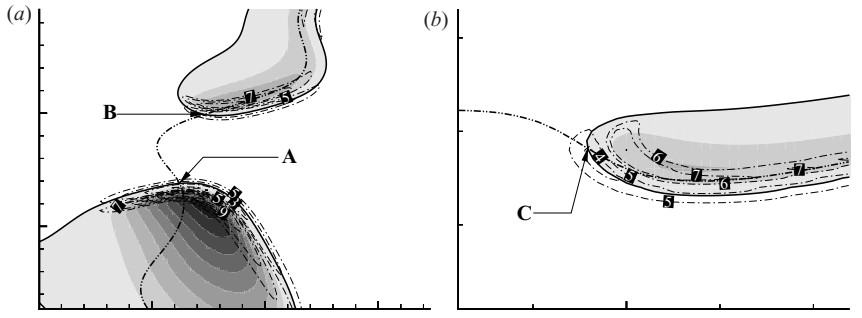

FIGURE 22. Close up of two typical edges and the associated hydrogen radical mass fraction (grey contourmap), stoichiometric line (thick dashed-double-dotted line), hydrogen radical mass fraction threshold (thick line) and hydrogen radical reaction rate (thin dashed-dotted line); (*a*) desirable case and (*b*) less desirable case. Hydrogen radical reaction rate isocontours are labelled with numbers from 1 to 12 and denoting the values −0.002, −0.0015, −0.001, −0.0005, −0.00025, 0.00025, 0.0005, 0.001, 0.0015, 0.002, 0.0025 and 0.003, respectively.

radical mass fractions that are able to detect the flame edges accurately for all times (in our simulation) owing to the unstationary nature of the flame. This range is given approximately by $0.16 < Z_o < Z_s = 0.2$ and $Y_o < 6 \times 10^{-5}$ in our case. Values outside this range tend to produce fictitious flame edges or failed to detect the edges altogether. The four cases described in this Appendix are given in table 3.

To illustrate the typical cases that were encountered in the simulation database, figures 22(*a*) and 22(*b*) show two-dimensional cuts of two typical situations with the thresholds of case (ii). The colour and line scheme is the following: grey isocontours denote the intensity of hydrogen radical mass fraction (from black, highest value, to white, lowest), the thick continuous line denotes the isoline corresponding to the thresholds of hydrogen radical for case (ii), the thick dashed-double-dotted line denotes the stoichiometric line on this plane and finally the dashed-dotted line denotes isolines of the hydrogen radical reaction rate. Figure 22(*a*) is a representation of the vertical plane that runs through the centre of the small hole shown in the frontal view of figure 5. Two edges are shown in this figure. The case shown in figure 22(*a*) is a desirable case from the point of view of edge detection, because there is a very sharp change of the hydrogen radical mass fraction, and the isosurfaces, mixture fraction and hydrogen radical form nearly orthogonal angles. Figure 22(*b*) shows another case where the quality of the edge detection is less good, in the sense that the angle between the two surfaces at the intersection point is rather small. These two figures depict the two typical situations that were observed in the simulation database. Figure 23(*a*) shows the hydrogen radical mass fraction through the vertical plane passing through the isosurface intersection, points A and B, of figure 22(*a*) and that through the horizontal plane at the intersection, point C, in figure 22(*b*). The threshold value is shown as a

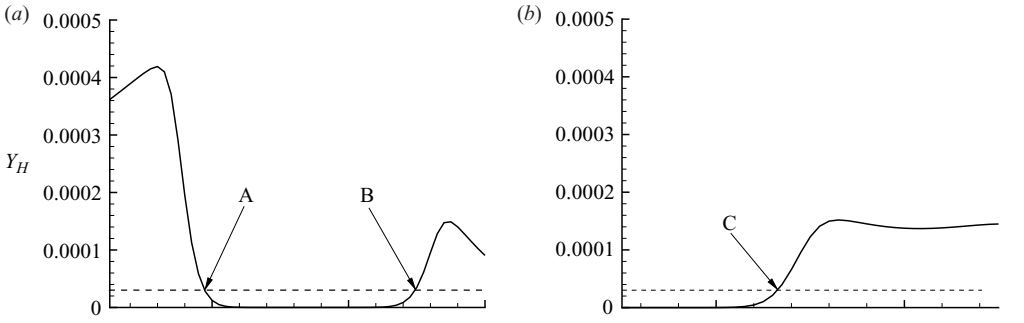

FIGURE 23. Hydrogen radical mass fraction variation across edges; (*a*) desirable case, (*b*) less desirable case.

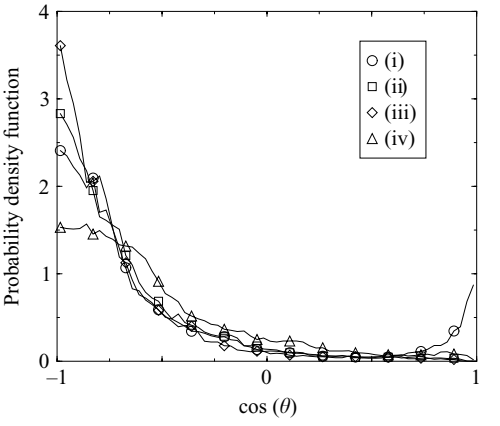

FIGURE 24. Probability density function of $\cos(\theta)$ for varying threshold parameters.

broken thick line. It can be seen that the threshold value gives a reasonable detection for the edges, while the threshold used in case (i), twice as high, is probably too high for the edges B and C. Nevertheless, the quality of the edge location is reasonable in both cases. Had we had chosen a higher threshold, we would have been penalized in the quality of the detection of cases like that shown in figure 23(*b*). Given these observations, it was deemed appropriate to use $Y_o = 3 \times 10^{-5}$ for the extraction of the statistics.

A quantity that is useful in assessing the quality of the edge detection is the distribution of angles between the mixture fraction isosurface and the hydrogen radical mass fraction isosurface, θ. Very small angles have large uncertainty because they correspond to surfaces that run almost parallel to each other. Figure 24 shows the p.d.f. of $\cos(\theta)$ for all cases in table 3. It is observed that the p.d.f. is mostly concentrated in the region $\cos(\theta) < 0$. Furthermore, depending on the threshold values, some p.d.f.s have appreciabe probability values at $\cos(\theta) = -1$. The samples that contribute to the p.d.f. at this location correspond, in the database, to flame hole formation events. They represent highly transient processes that cannot be detected easily because the flame edges have not formed yet. The flame is transitioning from its almost one-dimensional to a two-dimensional structure (in the plane of the edge). These events are associated with very large rates of scalar dissipation and extremely large edge velocities. Fortunately, they represent a small fraction of all the edges in the simulation and after some experimentation it was observed that we could

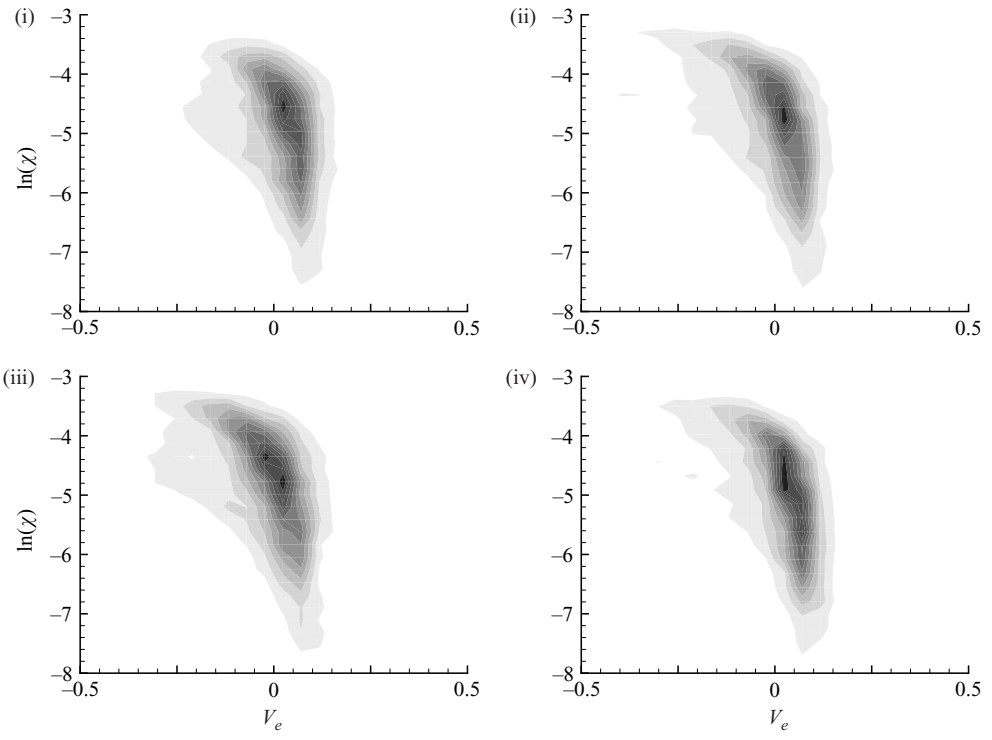

FIGURE 25. Joint p.d.f. of edge velocity-scalar dissipation for all four cases in table 3.

exclude most of these events by discarding the cases with $|\cos(\theta)| > \cos(\theta_o)$. We determined that $\theta_o = 10^\circ$ was a satisfactory choice that resulted in the exclusion of approximately 4% of the samples. As shown below, this procedure has negligible effect on the measured statistics and helps to produce smoother p.d.f.s by removing the contribution from the uncertain isosurfaces intersections.

Finally, the joint p.d.f. of flame-edge velocity and scalar dissipation using the different isosurface thresholds in table 3 are shown in figure 25. It is observed that all thresholds produce p.d.f.s that are qualitatively and quantitatively very similar; some small degree of statistical variability is unavoidable. Moreover, the fact that edges where $|\cos(\theta)| > \cos(\theta_o)$ have been excluded has a negligible impact on the statistics. This is the case here, because by altering the threshold value, Z_o, we also change the angle θ of each detected edge. By spanning the range of Z_o values, from 0.16 to 0.2, a good edge that is detected with a poor angle at a given threshold becomes well detected with a different threshold. A good edge is one that is well defined and it is not part of a hole formation event. Since the computed p.d.f.s do not change appreciably for different threshold values, we can conclude that our exclusion criteria based on θ remove most of the contributions from the ill-defined hole formation events.

REFERENCES

BAI, X. S. & SESHADRI, K. 1999 Rate-ratio asymtotic analysis of non-premixed methane flames. *Combust. Theory Modelling* **3**, 51–75.

BARLOW, R. S. & FRANK, J. H. 1998 Effects of turbulence on species mass fractions in methane/air jet flames. *Proc. Combust. Inst.* **27**, 1087–1095.

Baum, M., Poinsot, T. & Thévenin, D. 1995 Accurate boundary conditions for multicomponent reactive flows. *J. Comput. Phys.* **116**, 247–261.

Bédat, B., Egolfopoulos, F. N. & Poinsot, T. 1999 Direct numerical simulation of heat release and nox formation in turbulent nonpremixed flames. *Combust. Flame* **119**, 69–83.

Bergmann, V., Meier, W., Wolff, D. & Stricker, W. 1998 Application of spontaneous Raman and Rayleigh scattering and 2d lif for the characterization of a turbulent $CH_4/H_2/N_2$ jet diffusion flame. *Appl. Phys.* B **66**, 489–502.

Bilger, R. W., Stårner, S. H. & Kee, R. J. 1990 On reduced mechanisms for methane air combustion in nonpremixed flames. *Combust. Flame* **80**, 135–149.

Bogdanoff, D. W. 1983 Compressibility effects in turbulent shear layers. *AIAA J.* **21**, 926–927.

Boulanger, J. & Vervisch, L. 2002 Diffusion edge-flame: approximation of the flame tip Damköhler number. *Combust. Flame* **130**, 1–14.

Buckmaster, J. 1996 Edge-flames and their stability. *Combust. Sci. Tech.* **115**, 41–68.

Buckmaster, J. 2001 Large-Lewis-number instabilities of model edge-flames. *Combust. Flame* **127**, 2223–2233.

Buckmaster, J. 2002 Edge-flames. *Prog. Energ. Combust. Sci.* **28**, 435–475.

Buckmaster, J. & Jackson, T. L. 2000 Holes in flames, flame isolas, and flame edges. *Proc. Combust. Inst.* **28**, 1957–1964.

Buckmaster, J. & Matalon, M. 1988 Anomalous Lewis number effects in tribrachial flames. *Proc. Combust. Inst.* **22**, 1527–1535.

Buckmaster, J. & Short, M. 1999 Cellular instabilities, sublimit structures and edge-flames in premixed counterflows. *Combust. Theory Modelling* **3**, 199–214.

Card, J. M., Chen, J. H., Day, M. & Mahalingam, S. 1994 Direct numerical simulations of turbulent non-premixed methane–air flames modeled with reduced kinetics. *CTR Rep. Stanford University*, pp. 41–54.

Chelliah, H. K. & Williams, F. A. 1990 Aspects of the structure and extinction of diffusion flames in methane–oxygen–nitrogen systems. *Combust. Flame* **80**, 17–48.

Chen, L.-D., Roquemore, W. M., Goss, L. P. & Vilimpoc, W. 1991 Vorticity generation in jet diffusion flames. *Combust. Sci. Tech.* **77**, 41–57.

Clemens, N. T. & Paul, P. H. 1995 Effects of heat release on the near field flow structure of hydrogen jet diffusion flames. *Combust. Flame* **102**, 271–284.

Cook, A. W. & Riley, J. J. 1996 Direct numerical simulation of a turbulent reactive plume on a parallel computer. *J. Comput. Phys.* **129**, 263–283.

Dally, B. B., Karpetis, A. N. & Barlow, R. S. 2002 Structure of turbulent non-premixed jet flames in a diluted hot coflow. *Proc. Combust. Inst.* **29**, 1147–1154.

Daou, J. & Liñán, A. 1998 The role of unequal diffusivities in ignition and extinction fronts in strained mixing layers. *Combust. Theory Modelling* **2**, 449–477.

Dold, J. W. 1988 Flame propagation in a nonuniform mixture: the structure of anchored triple-flames. *Prog. Astro. Aero.* **113**, 240–248.

Dold, J. W., Hartley, L. J. & Green, D. 1991 Dynamics of laminar triple-flamelet structures in non-premixed turbulent combustion. In *Dynamical Issues in Combustion Theory* (ed. A. L. P. C. Fife & F. Williams), vol. 35, pp. 83–105. Springer.

Echekki, T. & Chen, J. H. 1998 Structure and propagation of methanol–air triple flames. *Combust. Flame* **114**, 231–245.

Everest, D. A., Driscoll, J. F., Dahm, W. J. A. & Feikema, D. A. 1995 Images of the two-dimensional field and temperature gradients to quantify mixing rates within a non-premixed turbulent jet flame. *Combust. Flame* **101**, 58–68.

Everest, D. A., Feikema, D. A. & Driscoll, J. F. 1996 Images of the strained flammable layer used to study the liftoff of turbulent jet flames. *Proc. Combust. Inst.* **26**, 129–136.

Favier, V. & Vervisch, L. 1998 Investigating the effects of edge flames in liftoff in non-premixed turbulent combustion. *Proc. Combust. Inst.* **27**, 1239–1245.

Ghosal, S. & Vervisch, L. 2000 Theoretical and numerical study of a symmetrical triple flame using the parabolic flame path approximation. *J. Fluid Mech.* **415**, 227–260.

Gibson, C. H. 1968 Fine structure of scalar fields mixed by turbulence. i. zero-gradient points and minimal gradient surfaces. *Phys. Fluids* **11**, 2305–2315.

Givi, P. 1989 Model-free simulations of turbulent reactive flows. *Prog. Energy Combust. Sci.* **15**, 1–107.

Im, H. G. & Chen, J. H. 1999 Structure and propagation of triple flames in partially premixed hydrogen–air flames. *Combust. Flame* **119**, 436–454.

Im, H. G. & Chen, J. H. 2001 Effects of flow strain on triple flame propagation. *Combust. Flame* **126**, 1384–1392.

James, S. & Jaberi, F. A. 2000 Large scale simulations of two-dimensional nonpremixed jet flames. *Combust. Flame* **123**, 465–487.

Jiménez, J. 2003 Computing high-Reynolds-number turbulence: will simulations ever replace experiments? *J. Turbulence* **4**, Paper 22.

Jou, W.-H. & Riley, J. J. 1989 Progress in direct numerical simulations of turbulent reacting flows. *AIAA J.* **27**, 1543–1556.

Karpetis, A. N. & Barlow, R. S. 2002 Measurements of scalar dissipation in a turbulent piloted methane/air jet flame. *Proc. Combust. Inst.* **29**, 1929–1936.

Kelman, J. B. & Masri, A. R. 1997 Reaction zone structure and scalar dissipation rates in turbulent diffusion flames. *Combust. Sci. Tech.* **129**, 17–55.

Kioni, P. N., Rogg, B., Bray, K. N. C. & Liñán, A. 1993 Flame spread in laminar mixing layers: the triple flame. *Combust. Flame* **95**, 276.

Klimenko, A. Y. & Bilger, R. W. 1999 Conditional moment closure for turbulent combustion. *Prog. Energ. Combust. Sci.* **25**, 595–687.

Ko, Y. S. & Chung, S. H. 1999 Propagation of unsteady tribrachial flames in laminar non-premixed jets. *Combust. Flame* **118**, 151–163.

Lele, S. K. 1992 Compact finite differences schemes with spectral-like resolution. *J. Comput. Phys.* **103**, 16–42.

Li, N., Balaras, E. & Piomelli, U. 2000 Inflow conditions for large-eddy simulations of mixing layers. *Phys. Fluids* **12**, 935–938.

Liñán, A. & Crespo, A. 1976 Asymptotic analysis of unsteady diffusion flames for large activation-energies. *Combust. Sci. Tech.* **14**, 95–117.

Livescu, D., Jaberi, F. A. & Madnia, C. K. 2002 The effects of heat release on the energy exchange in reacting turbulent shear flow. *J. Fluid Mech.* **450**, 35–66.

McBride, B. J., Gordon, S. & Reno, M. A. 1993 Coefficients for calculating thermodynamic and transport properties of individual species. *Tech. Rep.* TM-4513. NASA.

McMurtry, P., Riley, J. J. & Metcalfe, R. 1989 Effects of heat release on the large-scale structure in turbulent mixing layers. *J. Fluid Mech.* **199**, 297–332.

Mahalingam, S., Chen, J. H. & Vervisch, L. 1995 Finite-rate chemistry and transient effects in direct numerical simulations of turbulent nonpremixed flames. *Combust. Flame* **102**, 285–297.

Meier, W., Barlow, R. S., Chen, Y.-L. & Chen, J.-Y. 2000 Raman/Rayleigh/lif measurements in a turbulent $CH_4/H_2/N_2$ jet diffusion flame: experimental techniques and turbulence–chemistry interaction. *Combust. Flame* **123**, 326–343.

Mell, W. E., Nilsen, V., Kosály, G. & Riley, J. J. 1994 Investigation of closure models for nonpremixed turbulent reacting flows. *Phys. Fluids* **6**, 1331–1356.

Miller, R. S., Madnia, C. K. & Givi, P. 1994 Structure of a turbulent reacting mixing layer. *Combust. Sci. Tech.* **99**, 1–36.

Mizobuchi, Y., Tachibana, S., Shinio, J., Ogawa, S. & Takeno, T. 2002 A numerical analysis of the structure of a turbulent hydrogen jet lifted fame. *Proc. Combust. Inst.* **29**, 2009–2015.

Montgomery, C. J., Kosály, G. & Riley, J. J. 1997 Direct numerical solution of turbulent nonpremixed combustion with multistep hydrogen–oxygen kinetics. *Combust. Flame* **109**, 113–144.

Muñiz, L. & Mungal, M. G. 1997 Instantaneous flame-stabilization velocities in lifted-jet diffusion flames. *Combust. Flame* **111**, 16–31.

Muñiz, L. & Mungal, M. G. 2001 Effects of heat release and buoyancy on flow structure and entrainment in turbulent nonpremixed flames. *Combust. Flame* **126**, 1402–1420.

Pantano, C. 2004 A nonstiff additive semi-implicit Runge–Kutta scheme for finite-rate reacting flows. *J. Comput. Phys.* (submitted).

Pantano, C. & Lombeyda, S. 2003 Identification of flame edges from multispecies chemical compositional data. *Tech. Rep.* 197. Center for Advanced Computational Research, California Institute of Technology.

Pantano, C. & Pullin, D. I. 2003 On the dynamics of the collapse of a diffusion-flame hole. *J. Fluid Mech.* **480**, 311–332.

Pantano, C. & Pullin, D. I. 2004 A statistical description of turbulent diffusion flame holes. *Combust. Flame* (in press).

Pantano, C., Sarkar, S. & Williams, F. A. 2003 Mixing of a conserved scalar in a turbulent reacting shear layer. *J. Fluid Mech.* **481**, 291–328.

Papamoschou, D. & Roshko, A. 1988 The compressible turbulent shear layer: an experimental study. *J. Fluid Mech.* **197**, 453–477.

Peters, N. 1984 Laminar diffusion flamelet models in non-premixed turbulent combustion. *Prog. Energ. Combust. Sci.* **10**, 319–339.

Peters, N. 1985 *Numerical and Asymptotic Analysis of Systematically Reduced Reaction Schemes for Hydrocarbon Flames*. Lecture Notes in Physics, vol. 241, pp. 90–109.

Peters, N. 1986 Laminar flamelet concepts in turbulent combustion. *Proc. Combust. Inst.* **21**, 1231–1250.

Peters, N. 1991 *Reduced Kinetic Mechanisms and Asymptotic Approximations for Methane–Air Flames*, chap. 3. Springer.

Peters, N. & Kee, R. J. 1987 The computation of stretched laminar methane air diffusion flames using a reduced 4-step mechanism. *Combust. Flame* **68**, 17–29.

Phillips, H. 1965 *Proc. Combust. Inst.* **10**, 1277–1283.

Pitsch, H. 2000 Unsteady flamelet modeling of differential diffusion in turbulent jet diffusion flames. *Combust. Flame* **123**, 358–374.

Rehm, J. E. & Clemens, N. T. 1999 The large-scale turbulent structure of nonpremixed planar jet flames. *Combust. Flame* **116**, 615–626.

Roquemore, W. M., Chen, L.-D., Goss, L. P. & Lynn, W. F. 1987 The structure of jet diffusion flames. In *Turbulent Reacting Flows* (ed. R. Borghi & S. Murthy), pp. 49–63.

Ruetsch, G. R., Vervisch, L. & Liñán, A. 1995 Effects of heat release on triple flames. *Phys. Fluids* **7**, 1447–1454.

Santoro, V. S., Liñán, A. & Gomez, A. 2000 Propagation of edge flames in counterflow mixing layers: Experiments and theory. *Proc. Combust. Inst.* **28**, 2039–2046.

Schefer, R. W., Namazian, M., Filtopoulos, E. E. J. & Kelly, J. 1994 Temporal evolution of turbulence/chemistry interactions in lifted, turbulent-jet flames. *Proc. Combust. Inst.* **25**, 1223–1231.

Seshadri, K. & Peters, N. 1988 Asymptotic structure and extinction of methane–air diffusion flames. *Combust. Flame* **73**, 23–44.

Shay, M. L. & Ronney, P. D. 1998 Nonpremixed edge flames in spatially varying straining flows. *Combust. Flame* **112**, 171–180.

Short, M., Buckmaster, J. & Kochevets, S. 2001 Edge-flames and sublimit hydrogen combustion. *Combust. Flame* **125**, 893–905.

Smooke, M. D. & Giovangigli, V. 1991 *Reduced Kinetic Mechanisms and Asymptotic Approximations for Methane–Air Flames*, chap. 1, pp. 1–28. Springer.

Stanley, S. A., Sarkar, S. & Mellado, J. P. 2002 A study of the flow-field evolution and mixing in a planar turbulent jet using direct numerical simulation. *J. Fluid Mech.* **450**, 377–407.

Stårner, S. H., Bilger, R. W., Long, M. B., Frank, J. H. & Marran, D. F. 1997 Scalar dissipation measurements in turbulent jet diffusion flames of air diluted methane and hydrogen. *Combust. Sci. Tech.* **129**, 141–163.

Swaminathan, N. & Bilger, R. W. 1997 Direct numerical simulation of turbulent nonpremixed hydrocarbon reaction zones using a two-step reduced mechanism. *Combust. Sci. Tech.* **127**, 167–196.

Swaminathan, N., Mahalingam, S. & Kerr, R. M. 1996 Structure of nonpremixed reaction zones in numerical isotropic turbulence. *Theor. Comput. Fluid Dyn.* **8**, 201–218.

Takahashi, F., Schmoll, W. J., Trump, D. D. & Goss, L. P. 1996 Vortex–flame interactions and extinction in turbulent jet diffusion flames. *Proc. Combust. Inst.* **26**, 145–152.

Thatcher, R. W. & Dold, J. W. 2000 Edges of flames that do not exist: flame-edge dynamics in a non-premixed counterflow. *Combust. Theory Modelling* **4**, 435–457.

Vedarajan, T. G. & Buckmaster, J. 1998 Edge-flames in homogeneous mixtures. *Combust. Flame* **114**, 267–273.

Vervisch, L. & Poinsot, T. 1998 Direct numerical simulation of non-premixed turbulent flames. *Annu. Rev. Fluid Mech.* **30**, 655–691.

Wall, C., Boersma, B. J. & Moin, P. 2000 An evaluation of the assumed beta probability density function subgrid-scale model for large eddy simulation of nonpremixed, turbulent combustion with heat release. *Phys. Fluids* **12**, 2522–2529.

Williams, F. A. 1975 Recent advances in theoretical descriptions of turbulent diffusion flames. In *Turbulent Mixing in Non-reactive and Reactive Flows* (ed. S. Murthy), pp. 189–208. Plenum, New York.

Williams, F. A. 1985 *Combustion Theory*. Benjamin/Cummings, Menlo Park, CA .

Yamashita, H., Shimada, M. & Takeno, T. 1996 A numerical study on flame stability at the transition point of jet diffusion flames. *Proc. Combust. Inst.* **26**, 27–34.

Yule, A. J., Chigier, N. A., Ralph, S., Boulderstone, R. & Ventura, J. 1980 Combustion-transition interaction in a jet flame. *AIAA J.* **19**, 752–760.